People's Democratic Republic of Algeria

Ministry of Higher Education and Scientific Research

University Abderrahmane MIRA of Bejaia

Faculty of Technology

Department of Hydraulics

Applied Hydraulics and Environment Research Laboratory (AHERL)

FINAL DEGREE PROJECT

Presented by:

LYDIA HADRI

Submitted for partial fulfilment for the **MASTER** degree in **Hydraulics**

Option: Hydraulic Structures and Facilities.

Title
Analysis of Dam Break problem with an elastic obstacle using Particle Finite Elements Method

Graduated on 03/07/2023

Project committee :

President : A. Bedjou

Examiner(s) : F. Nait Bouda

Advisor : A. Seghir

Academic year 2022/2023

Acknowledgements

Abstract: The aim of this project is to analyse the well-known example of the fluid-structure interaction, the phenomenon of dam break with a flexible obstacle. The Navier-Stokes equations have been analysed using the Particle Finite Element Method and the obstacle is considered as a 2D beam finite elements. The numerical simulations have been carried out using the OpenSeesPy script and and the post-processing have been performed using ParaView. In this work, different concepts related to this object have been discussed and explained in order to get a deeper knowledge of the subject.

Keywords: Dam-Break, Particle Finite Element Method, Finite Element Method, Numerical simulation, Navier-Stockes equations, flexible obstacle, OpenSees, ParaView.

Résumé : L'objectif de ce projet est d'analyser un exemple bien connu de l'interaction fluide-structure, le phénomène de rupture de barrage contre un obstacle flexible. Les équations de Navier-Stokes ont été analysées avec la méthode des éléments finis particulaires et l'obstacle est considéré comme des éléments de poutre 2D. Les simulations numériques ont été réalisées à l'aide du script OpenSeesPy et et les post-traitements ont été fait avec ParaView. Dans ce travail, différents concepts liés à cet objet ont été discutés et expliqués afin d'avoir une connaissance plus approfondie du sujet.

Mots clés : Rupture de barrage, Méthode des éléments finis particulaire, Méthode des éléments finis, Simulation numérique, obstacle flexible, OpenSees, ParaView.

Contents

List of Figures

Nomenclature

Variables

A	Cross section
C^n	Cloud of nodes
E	Modulus of elasticity of the beam [kPa]
f_i	Source term (normally the gravity) [m/s^2]
F_p	Total Force due to Pressure [N]
F_v	Total Force due to velocity [N]
f_i	Source term (normally the gravity) [m/s^2]
g	Gravity [m/s^2]
H_c	Container length [mm]
H_f	Fluid initial length [mm]
H_e	Elastic obstacle (Beam) length [mm]
H_c	Rigid obstacle length [mm]
h	Cell size [mm]
h(x)	Minimum distance between two particles
I_z	Moment of inertia [$kg.m^2$]
k	Iteration counter
L	Length [m]
L_c	Container width [mm]
L_f	Fluid initial width [mm]
L_c	Rigid obstacle width [mm]
M	Moment
M^n	Finite Element Method mesh
P	Pressure [Pa]
P_0	Fluid initial Pressure [Pa]
P_i	Pressure value at the point of height Y_i [Pa]

P_{max}	Maximum Pressure value [Pa]
q	Transverse load
T	Shear force [Pa]
T_i	Vernoi cell
t	Time [s]
u_0	Fluid initial velocity [m/s]
u_f	Fluid velocity
u_i	Cartesian components of the velocity field
u_i^*	Fractional velocity
u_s	Solid velocity
V	Volume [m^3]
V^n	Fluid and solid domain
v	Displacement in the y direction
v_{xi}	Horizontal velocity along the Beam at the given time [m/s]
v_i	Component of normal vector
x_f	Fluid displacement
x_s	Solid displacement
x	Horizontal displacement of the Beam [m]
Y	Vertical displacement of the Beam [m]
Y_i	Vertical points along the cut line [m]
y	Distance from the centre of the section

Greek symbols

α	Alpha parameter in alpha-shape method
Δt	Time increment
δ_{ij}	Kroncker delta
ϵ_x	Axial strain in the x direction
ζ_i	Components of tangent vector
θ	Angle of rotation
Γ_f	Fluid boundary
Γ_s	Solid boundary
γ	Parameter giving the amount of pressure split
ν	Poison relation
μ	Dynamic viscosity [$Pa.s$]
ρ^*	Fractional density
ρ_f	Fluid Density [kg/m^3]
ρ_s	Solid Density [kg/m^3]
τ_{ij}	Deviator stress tensor

Acronymes

ALE	Arbitrary Lagrangian-Eulerian
CFD	Computational Fluid Dynamics
CSM	Computational Structural Mechanics
DOF	Degree of freedom
DPD	Dissipative Particle Dynamics
EDT	Extended Delaunay Tessellation
FEM	Finite Element Method
FSI	Fluid Structure Interaction
FVM	Finite Volume Method
LBM	Lattice Boltzmann Method
MAC	Modal Assurance Criterion
MD	Molecular Dynamics
MFEM	Meshless Finite Element Method
MPS	Moving Particle Semi-implicit
NSE	Navier-Stokes Equation
PFEM	Particle Finite Element Method
RKPM	Reproducing Kernel Particle Methods
SLC	Semi Lagrangian Contouring
SM	Spectural Method
SOLA	SOLution Algorithm
SPH	Smoothed Particle Hydrodynamics
VOF	Volume Of Fluid

Introduction

Fluid dynamics is governed by the Navier-Stokes equations, a set of coupled and non-linear partial differential equations derived from the fundamental law of conservation of mass and momentum that describe the flow of incompressible fluids, where the unknowns are usually velocity and pressure. The equations are a generalisation of those developed by the Swiss mathematician L. Euler to describe the flow of incompressible and frictionless fluids. Later, the French engineer C.L. Navier introduced the element of viscosity (friction) for the more realistic and much more difficult problems of viscous fluids. The British physicist/mathematician Sir G.G. Stockes improved on this work, but only obtained complete solutions for simple 2D flows. The complex turbulence and vortexes, that occur in 3D fluid flows as velocities increase have been shown to defy all but the most approximate numerical analysis methods. The problem with these equations is that they are not yet analytically solvable. In this case, scientists have turned to theoretical and experimental methods, and today, with the rapid and enormous technological developments in computers and software, to computational fluid dynamics.

Computational Fluid Dynamics (CFD) is a numerical approximation of real physics in computers. It has become an essential skill for engineers, allowing them to understand the details of how fluids behave in motion, and facilitating their study in a computer before a prototype is built. The cost of CFD analysis continues to decrease as computers become more powerful and software uses more efficient algorithms. Reduced cost, satisfactory accuracy and short lead times ensure that virtual prototypes can be calculated at the same time as physical prototypes. There are many commercially available programs that are easy to use, but require a deep understanding of fluid mechanics concepts to allow the engineer to judge the adequacy of the result. The accuracy of CFD depends on the mesh size and the quality of the numerical methods, which describe different problems in different ways, and its central process is the reduction of infinite-degree of freedom differential equations to finite-degree of freedom systems [38, 3].

There are many numerical methods for solving deferential equations, all of which approximate a differential equation governing a variable u into a set of algebraic equations of the matrix K.U = F. Finite difference and finite volume methods come to mind, but they're not the only ones, they're just a few of many. CFD numerical methods are classified as either Eulerian or Lagrangian, and the difference lies in the way their inventors view and observe the flow of fluids. This also generally termed mesh and particle methods, mesh methods are mostly with a Eulerian point of view and there is a numerous methods in this class such as those mentioned above (FDM and FVM) in addition to them, Finite Element Method, Lattice Boltzmann Method, while particle methods are with a Lagrangian point of view methods in this category Moving Particle Semi-implicit (MPS), Smoothed Particle Hydrodynamics (SPH) and Particle Finite Element Methods (PFEM) that received enormous recognition. PFEM is also known as the mesh and particle method because it solves the governing equations using the finite element method, also known as the mesh method.

Proposed by Oñate & Idelsohn, PFEM was originally designed for fluid dynamics and fluid-structure interaction problems, but soon extended to solve non-linear solid mechanics problems and to various fields of engineering and technology. The method's domain is defined by a collection of particles moving in a Lagrangian framework whose governing equations are solved by FEM. This numerical tool requires a fast regeneration of the mesh at each time step, which is carried out by the Extended Delaunay Tessellation, producing a convex figure that doesn't respect the internal and external physical boundaries, that is why the Alpha Shape technique is applied to identify isolated particles outside the main fluid domain.

The natural and hydraulic phenomenon of dam break is often used to validate the test for numerical simulations. Given the range of phenomena involved, including violent impacts with and between fluid masses, wave formation and movement, in addition to the stages of energy dissipation that can be identified before stable hydrostatic equilibrium is reached, it can be argued that a numerical model that can cope with the dam break flow is also capable of accurately simulating slower and less severe flows.

The paper is divided in four chapters, complemented by an introduction and conclusion. **Chapter 01** covers some of the basic concepts of fluid mechanics in CFD. A bibliography is provided with a summary of the studies related to the concepts.
Chapter 02 deals with numerical modelling by means of the particle finite element method, which is the main numerical tool used in this project. The numerical technique is explained in detail by reference to papers published by its inventors, Oñate & Idelsohn.
Chapter 03 discusses with the modelling of the beam element by the finite element method. The beam being part of the fluid-structure interaction simulation case, it is discussed from the generation of the governing equation to the derivation of the elementary matrices.
Chapter 04 reveals the numerical simulation using a PFEM based software OpenSees. Two cases of dam break are visualised with ParaView, one being a dam break with a rigid wall and the other, a popular FSI model, a dam break against an elastic obstacle, i.e. a beam.

Research Review

1.1 Introduction

The purpose of this chapter is to provide an introduction to some of the important fluid mechanics concepts used in CFD. Approaches and numerical methods are defined along some of the main notions that will be dealt with in this project. This gives a brief and generalised insight into the field of modelling and analysis of fluid flows.

1.2 Lagrangian Approach

The Lagrangian description, in which a particular region of fluid is identified and tracked, forms a ¨closed system¨ that moves and deforms with the flow, but no mass ever crosses the material volume surface, i.e. the volume of fluid changes shape while the total mass remains constant. Unlike the Eulerian observer, the Lagrangian observer stays with each fluid element or material volume and records its fundamental changes as it moves through space. In the Lagrangian approach, the mesh of the computational domain moves with the velocity of the fluid particles, and the motion of the mesh can also lead to element entanglement. However, it's computationally expensive to keep track of the trajectories of all the fluid particles in a flow, so the Lagrangian description is only used in some numerical simulations and is preferred for problems with small motions[41, 28].

Simply put, the Lagrangian approach is the process of describing the entire flow by recording the detailed history of each fluid particle. The Lagrangian observer, using a plain example of a flowing river, is the one who dives into the river and then looks around as he or she drifts with the current.

1.3   Eulerian Approach

Eulerian description, where attention is focused on a given volume in space. The volume is fixed with respect to a set of reference points, and the fluid is studied as it passes through the fixed volume, continuously renewing itself within it. In the Eulerian framework, an ¨open system¨ is considered in which mass, momentum and energy can easily cross, i.e. be transported over the surface of the control volume, and local changes in fluid flow can occur within the control volume over time. The fixed or moving control volume may be a large or small finite volume generated by a computational mesh, or it may be in the limit a ¨point¨ in the flow field. Generally, the Eulerian observer fixed to an inertial reference frame records the temporal and spatial changes of the flow field at all ¨points¨, or in the case of a control volume, the transients inside and across its control surfaces [41, 28].

In simple terms, the Eulerian approach is about recording the evolution of the flow properties at any point in space as time varies. The Eulerian observer, using the same example of a flowing river as before, is the one who prefers to observe the river while standing still.

1.4   Arbitrary Lagrangian Eulerian Approach

Due to the shortcomings of both the pure Eulerian and the pure Lagrangian description, a generalised technique has been developed which allows to combine at best interesting aspects of the classical mesh description, while minimising their disadvantages as far as possible. Such a technique is called the Arbitrary Lagrangian Eulerian description, which uses a referential domain for the description motion, different from the material domain (Lagrangian description) and the spatial domain (Eulerian description).

ALE was first developed in the finite difference and finite volume contexts. In the ALE description, the nodes of the computational mesh can be moved with the continuum in normal Lagrangian fashion, or held in Eulerian manner, either moved in some arbitrary specified way to give a continuous rezoning capability; this freedom allows greater, distortion of the continuum to be handled than would be allowed by a purely Lagrangian method, with greater resolution than is possible with a purely Eulerian approach. Therefore, one of the main problems with the ALE description is that the mesh nodes move at an arbitrary speed. Different techniques have been developed to update the mesh in fluid motion, depending on the fluid domain. For problems defined in a simple domain, the mesh velocity can be derived from the uniform or non-uniform distribution of nodes along straight lines ending at the moving boundaries. The purpose of ALE algorithms, is to provide a capability for automatic rezoning that conserves the regularity of the computational mesh, something that makes the algorithms particularly useful for flow problems with large, distorted boundaries that are mobile and deforming[12, 41, 32, 39].

1.5   Particle-based Methods

Particle methods are a widely used class of numerical algorithms in scientific comput-ing, they are said to be new and advanced against the conventional mesh-based methods. Their applications range from CFD to MD. They are based on Lagrangian description and mesh-less discretisation to simulate continuum mechanics. Many particle methods have been developed, some of which are listed below: Dissipative Particle Dynamics (DPD), Repro-ducing Kernel Particle Methods (RKPM), Moving Particle Semi-implicit (MPS), Smoothed Particle Hydrodynamics (SPH) and Particle Finite Element Methods (PFEM), which have received significant recognition for their results[31]. The last two are explained below:

1.5.1   Smoothed Particle Hydrodynamics

First introduced in 1977 for astrophysical simulations, Smoothed Particle Hydrodynamics (SPH) is a discrete meshless Lagrangian technique in which the fluid volume is divided into a finite number of particles, whose position is not fixed, which have material properties and interact with each other within the range controlled by the weight or smoothing function. The basic concepts of this method is shown in Figure 1.1. Currently, SPH is a numerical technique used in many different fields, from astrophysics to engineering applications to biological flows, as it has seen a lot of progress in these years. The discretisation of the governing equations is based on these discrete particles, and a variety of particle-based formulations have been used to calculate the local density, velocity and acceleration of the fluid, while the fluid pressure is calculated from the density using an equation of state, and the particle acceleration is then calculated from the pressure gradient and the density. In SPH, the motion of the particles and the fluid surfaces or fluid-fluid interactions move the particles, representing their phase as defined in the initial stage [14, 46, 34].

Based on [33], the author has detailed on the advantages and weaknesses of SPH as he praised the technique for these: a free surface or interface is automatically followed and does not require special treatment, the method is inherently mass conservative, dynamic body interaction is handled automatically since the formulation is Lagrangian, fluid properties associated with different phase can be easily incorporated and also the method has well characterised numerical stability; while he indicated that SPH is still subject of several research and studies for some disadvantages that still has to be resolved in-listing: Low convergence rate, approximation of boundary conditions, large pressure fluctuations due to spurious pressure wave in the untreated weakly compressible formation, high computational cost and formation of voids.

SPH, has proven to be a valid alternative to the mesh-based methods, leading it to re-ceive wide interest in the last decades, where various modifications have been proposed to upgrade the original one, have a look at [47], there will be more details about it.
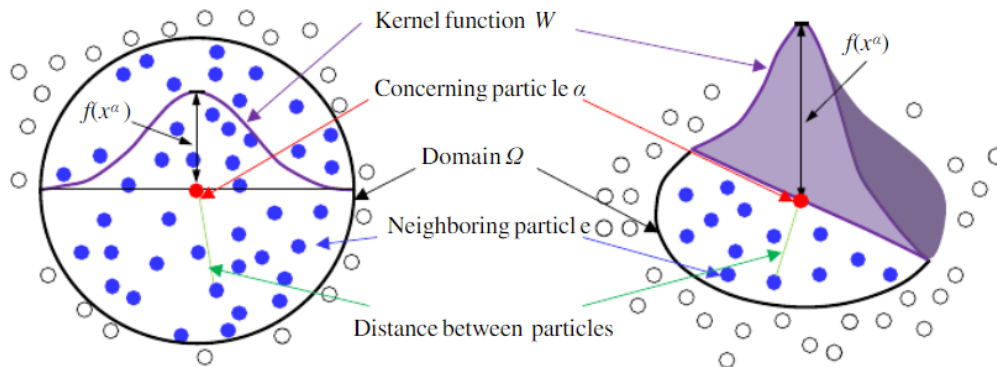
Figure 1.1: The concept of SPH [11].

1.5.2   Particle Finite Element Method

The Particle Finite Element Method is a numerical tool originally developed for fluid dynamics and fluid-structure interaction problems, but soon extended to solve non-linear solid mechanics problems and to various fields of engineering and technology. Its basic idea is to combine a Lagrangian finite element with an efficient and fast remeshing procedure.

In the PFEM, the Lagrangian framework is used to describe the motion, according to this description the mesh nodes, where all the information is stored, are treated as physical particles, this method discretises the physical domain with a mesh on which the differential governing equations are solved with a standard finite element approach, it also uses Delaunay triangulation to regenerate the mesh connectivity and the identification of external and internal boundaries is done by a specific technique called Alpha shape technique.

Specifically, a typical Particle Finite Element Method solution involves the following steps: First step, the domain is filled with a set of points called particles; second step, the external and internal boundaries of the computational domain are identified by the Alpha shape technique; then third step, the fluid and solid domains are discretised with a mesh generation scheme called Delaunay triangulation; this leads to the solution of the Lagrangian form of the governing equations; after that, the position of the nodes is updated and the last step is to go back to the first step and repeat the solution for the next time step [10].

The simulation software most often mentioned when discussing PFEM is OpenSees (the Open system for earthquake engineering simulation), which was originally developed as a computational platform for performance-based earthquake engineering research at the Pacific Earthquake Engineering Research Centre, To find out more, go to[44, 49].

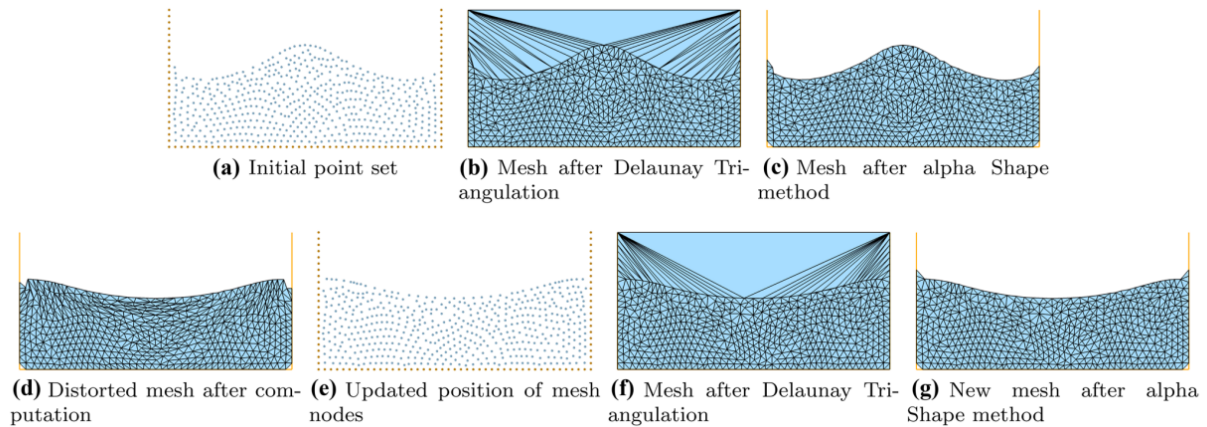**(a)** Initial point set   **(b)** Mesh after Delaunay Tri-angulation   **(c)** Mesh after alpha Shape method

(d) Distorted mesh after computation   **(e)** Updated position of mesh nodes   **(f)** Mesh after Delaunay Triangulation   **(g)** New mesh after alpha Shape method

Figure 1.2: Steps of Particle Finite Element Method[10].

1.6   Mesh-based Methods

The computational modelling of fluid dynamics systems requires the solution of the problems expressed in the Navier-Stocks equations, the solution of which has yet to be achieved, Numerical methods are used to reduce the complexity of the partial differential equations that will help to decrease the computational complexity involved in CFD. One family of these methods involves the discretization of space into regular grids or meshes. The most commonly used mesh-based methods are the Finite Element Method (FEM) and the Finite Volume Method (FVM). There are, of course, a variety of other numerical methods such as the Finite Difference Method (FDM), the Lattice Boltzmann Method (LBM), the Spectural Method (SM) and many more. A simple description of the first two methods is given here:

1.6.1   Finite Element Method

The Finite Element Method is one of the most powerful numerical techniques in solving complex systems of differential equations, which offer the possibility of developing a program that gives relatable solution for various engineering problems in particular complex form of geometric domain where the problem is well represented in all boundary conditions.

The majority of engineering problems are described by partial differential equations with boundary conditions defined on a domain and its contour. FEM is applied in five steps; the first is the formulation of the governing equations and boundary conditions, which requires a rewriting of these equations in integral form, where the weak formulation is usually used to include the boundary conditions. The second step is to divide the physical domain into several subdomains called finite elements and to calculate the connectivities of each of them and their nodes. The third take in approximating the variables of each element by simple linear, polynomial function, where the degree of polynomial interpolation is relied on the number of elements nodes. As for the fourth step is assembling all the elements properties

to form an algebraic system for the nodes physical variables values, and apply the boundary conditions to build the global matrix. The last step is to solve the global system, which defines either an equilibrium problem, which concerns a stationary or static case, or a problem of system values and vectors, generally the frequencies and modes of a physical system[40].An example of a meshed structure using FEM is shown in the following Figure 1.3, where the elements and nodes are shown.

The rapid growth of computer hardware and software technology over the last few decades has led to the creation and development of many commercial CFD software packages based on FEM, such as ANSYS mechanical, OpenFOAM, COMSOL, ADINA and many others, which have delivered visible results on problems such as FSI[26].
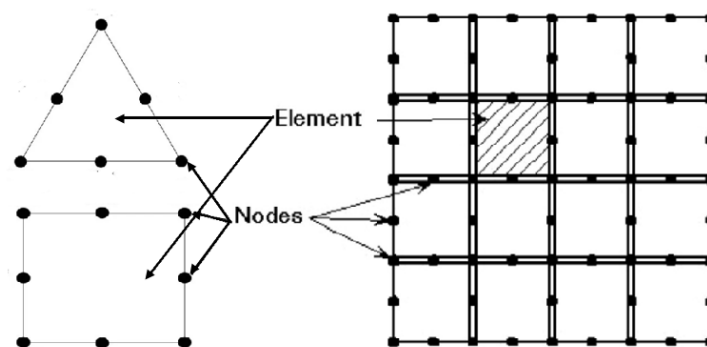
Figure 1.3: Elements & nodes in FEM [2].

1.6.2   Finite Volume Method

The finite volume method, also known as the control volume method, is a numerical technique used mainly in the simulation of fluid flow problems and related transport phenomena, where the basic idea is to divide the computational domain into discretised, non-repeating control volumes. The governing equations (differential equations) are integrated to obtain a set of discrete equations to be solved over each control volume. The coefficients of the discrete equations are calculated from the values in the cell centre and its neighbours, so it's important to keep the number of neighbouring cells as close together as possible. In summary, the main concept is that FVM acts as a transformer in fluid dynamics simulations, taking the control equations with boundary and mesh configurations as inputs. The resulting outputs are discretised sparse linear systems. To solve this linear system Ax=b, the continuous governing equations must be solved discretely on a mesh. Usually the internal mesh file contains the unstructured grid. This means that the internal meshes in the domain of interest do not have exactly the same neighbouring cells. As shown in Figure 1.4, (a) is a structured mesh and (b) is an unstructured mesh. To identify each element, a number or identity must be assigned to each node, volume, cell and surface. The number determines the order of assembly and the structure of the resulting matrix [48].

The commonly used commercial codes software based on FVM are ANSYS Fluent, Open FVM, YHACT and many others, which are widely used for engineering fluid flow simulation due to their accuracy, robustness and convenience[26].
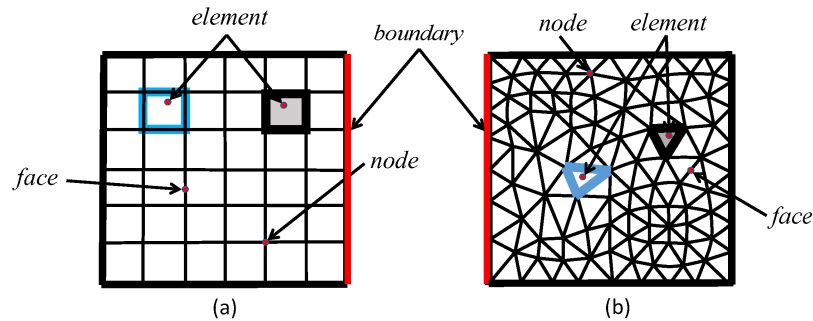

Figure 1.4: Domain discretised by: (a) uniform grid system, (b) unstructured grid system[48].

1.7   The Two Phase Flow

Two-phase flow is a special type of flow problem in which the mechanics of two phases of matter are considered at once. It is well known from the macroscopic description of matter that it can be classified into three states: solid, liquid and gas. Unlike the solid state, the other two states can be deformed without applying any force, provided that the deformation is sustained over a sufficiently long period of time, hence the term fluid has been used as a general term for these two phases. In classical fluid mechanics, the flow problems of a homogeneous fluid are treated in only one state, i.e. either liquid or gas. In such problems, the solid bodies in the flow field are usually assumed to be rigid bodies, so that the solids can be considered as given boundary conditions of the fluid flow problems. Although, in many engineering problems, as well as fluid flow in matter, the flow problems of a mixture of substances have to be treated in different states, and the solid bodies can not be considered as rigid bodies of given shape, such a system can generally be called the multi-phase[36]

Two-phase flow is a very complex physical phenomenon in which many types of flow can be found (gas-solid, gas-liquid, liquid-liquid...) and within each of these types several flow regimes can exist (annular flow, jet flow, slug flow, bubble flow, etc...). In addition, it has very complex physical laws and the mathematical treatment of the phenomena occurring in the presence of the two phases (inter-dynamic coalescence, break-up, drag,...) remains largely undeveloped. For this reason, there is still no agreement on the governing equations. Furthermore, the proposed constitutive models are empirical, but often lack experimental validation for the conditions under which they are applied, and the numerical solutions for solving the governing equations and closure laws of two-phase flows are extremely complicated, very often two-phases show inherent oscillatory behaviour, requiring costly transient solution algorithms. For these reasons, there is a lack of fundamental knowledge about two-phase flows and general CFD codes are not available.

Despite the major difficulties previously stated, significant progress has been made in various areas of two-phase flow. During the last two decades, various empirical correlations and phenomenological models have been proposed for the prediction of stratified gas-liquid flow characteristics. Given the gas and liquid flow rates, the global determination of both pressure drop and phase distribution (gas holdup) will be strongly dependent on the momentum transfer modelling. In a global approach to the problem, it is then necessary to propose three closing relations to express the momentum transfer coefficients.

The wall friction factor in the gas phase is generally well predicted by extrapolation of the classical relations derived in single phase flow. The wall friction factor in the liquid phase can be exported from the single phase relation as long as the liquid fractions are not too small. The main key to the modelling lies in the expression of the interfacial momentum transfer, which is closely related to the deformation of the gas-liquid interphase. For smooth stratified flow, there is no problem in expressing the corresponding smooth friction factor. For wavy stratified flow two approaches can be taken: Either a global empirical correlation for the interfacial friction factor can be proposed, or else the analogy to shear flow over a rough interface can be considered and at least an empirical correlation for the interfacial roughness can be proposed [15].

That said, with the technological development of today, many numerical methods are presented for solving numerically the descriptive equations, which are in the form of differential or integral equations, which produce testable predictions and allow analysis of the two-phase system variables, leading to a deeper understanding and the ability to develop new or improved system designs; the well-known modelling methods are the Finite Element Method and the Finite Volume Method, but there is also the Particle Finite Element Method, which is used in this project and is reported to give good results for this flow problem. Typically, the answer to a given flow problem is obtained by copying suitable equations, sub-models and boundary conditions with their appropriate solution technique from available sources[28].

1.8   Surface Tracking Techniques

With the different simulation problem various surface tracking techniques were developed to provide compelling advantage like detailed and visually pleasing results for the simulation methods, such techniques as:
Classical Metaballs: Are widely used type pf deformable implicit surface, which its visualisation is aimed at representing a whole nonrigid objects, ranging from soft bodies to water and gaseous phenomena. Its concept is closely related to the idea of Smoothed Particle Hydrodynamics (SPH), a convention used for simulating fluids as cloud of particles. Both methods apply smooth scalar function, that map points in space to a mass density.

Front Tracking Method: It explicitly discretise the free surface using particles and stored a connectivity between them. Generally a front structure consists of points connected by elements. The linked list structure is used to store both the points and elements, that contains pointers to the previous object and the next object in the list, that its order is completely arbitrary and has no connection to the actual order on the interfaces.

Point Set Method: To avert the adversity when free surface undergoes large deformations or topological changes. The mechanism varied from the standard Front Tracking process, where the indicator function is calculated from the surface normal.

Marching Cube Algorithm: The two primary steps in this approach for surface construction problem is locating the surface corresponding to a user specified value and create triangles constituted in the first step and the ensure a quality image of surface by calculating the normal to the surface at each vertex of each triangle. **Screen Space Mesh approach**: Introduced foe the generation of surfaces defined by the boundary 3D point clouds. A depth map with internal and external silhouettes was first generated in screen space the it's used to construct a 2D screen space triangle mesh with a technique derived from marching squares.

VOF and SOLA : Topological changes of the fluid surface were efficiently handled in VOF method which usually walk in the marching cubes algorithms. A light weight version of the basic algorithm SOLA uses the MAC method, but failed to treat free surfaces. An alternate mesh version of the SOLA code named SOLA-VM, was chosen as a fundamental for representing the VOF technique. The new experimental version is called SOLA-VOF.

Level Set Method: Liquid surfaces can be efficiently represented using the level set method and the dynamic implicit surface. A signed distance field $\Phi(X)$ explicitly points to the liquid surface and that could be defined as the shortest distance from position x to the liquid surface, so this surface of the liquid is characterised by a zero contour of the signed distance field. Velocity field u(x) derived from the Navier-Stokes equations used for the simulation. Level Set equation is solved by using upwind schema generates the implicit liquid surface.

Semi Lagrangian Methods: Have been extensively used in computer graphic community to solve the nonlinear advection term of Navier-Stockes equations. The SLC modifies its signed distance field by Semi-Lagrangian fashion and hence the triangle meshes extracted by Marching Cube and explicit polygon meshes with volume conservation, adoptive resolution, also an easy surface property convection.

Level Contour Reconstruction Method: As the interface stretches and deforms greatly in the simulations it's prime to add and remove the interface elements during solving period, so this method must be allowed to recombine when either parts of the similar interface or part of two separate interfaces came together.

Fluid Simulation and surface tracking are two different type of problems can be done without tracking but in order to add minute details, it will help a lot, and it can also be used as deformation tools [42].

1.9   Elasticity (Deformable Solid)

Elasticity is a property of matter where atomic forces in matter act to restore the shape of a solid when distorted by the application of external forces causing the deformations; also said to be the ability of a deformed material body to return to its original shape and size when the forces causing the deformation are removed[6].

Materials are elastic when external forces do not exceed the elastic limit. Beyond the elastic limit, solids can exhibit elastic behaviour and associated heat dissipation. Such non-elastic behaviour in solids occurs when they are subjected to strong external forces, which can be divided into two classes: body forces, such as gravity, which act on each element of the volume, and surface forces, which are forces acting on both sides of each infinitesimal surface element within the solid[8].

The main characteristic of elastic solids is the reversibility of all transformations after the removal of the loads that caused them, which manifests itself first in the recovery of the shape and second in the complete recovery of the energy transferred to the solid[18].

1.10   Fluid Structure Interaction

A flexible solid structure contacting a flowing fluid is subjected to a fluid stress which may cause deformation in structure, which in return changes the boundary conditions of the fluid system; it can also happen the other way around where the structure exercise a pressure that makes the fluid flows properties to change. This kind of interactions called Fluid-Structure Interaction (FSI), which is also a multi-physics phenomenon that occurs in many natural phenomena and men-made engineering systems. It becomes a crucial consideration in the design and analysis of various engineering systems. In a broad sense, Fluid-Structure Interaction covers such subjects as aero-elasticity, hydro-elasticity, flow-induced vibration, thermal deformation, etc...

FSI can be classified as either strongly or weakly coupled systems; FSI is identified as weakly coupled when a structure is in the flow field or containing flowing fluid deforms slightly or vibrates with small amplitude, it will effect negligibly the flow field because of the relatively two pressure. And called strongly coupled systems when the alteration of the flow field due to large deformation or high amplitude vibration of the structure can not be neglected, in such strongly coupled FSI systems in which large structural deformation or displacement results in a significant alteration of the original flow field, both altered and original flow field can not be linearly super-imposed open each other.

The governing equations with the inter-facial boundary conditions for a simple Fluid-Structure Interaction problem are too complex to address with analytical approach. Up to present most cases fluid and structure systems have been solved separately; however, there are special problems which are too complex and strong in coupling to solve the two systems

separately, in this cases technical advancement in the field of computational fluid dynamics (CFD), Computational Structure Mechanics (CSM) and numerical algorithms have made the numerical FSI analysis more realistic to be performed in a reasonable time frame.

Recently, many commercial software and several numerical approaches to solve highly complex non-linear problems have been developed and established to simulate FSI problems, we can mention some COMSOL, ANSYS Fluent, and OpenSees[27, 37].

1.11   The Dam-break problem

Dams are artificial or natural structures (caused by the accumulation of material as a result of ground movement) built across the bed of a watercourse that retain or are capable of retaining large volumes of water and have been essential to human development since ancient times because of their ability to control floods and subsequently use the stored water for drinking and irrigation. Artificial dams must be built in geologically sealed basins and consist of a body designed specifically for each type of structure, resting on a watertight foundation or made watertight upstream. This will involve additional structures such as spillways, water intakes, turbines, bottom outlets, etc. Today, as a result of technological advances, it has become possible to build larger dams to meet the growing demand for water and also to generate electricity and energy. As a consequence, major disasters when dams break, especially in in downstream inhabited cities.

Dam break therefore corresponds to the partial or total destruction of the structure, which leads to the formation of a submergence wave, resulting in a sudden rise in the water level downstream, even to a gigantic torrent.This flow is a typical example of an unsteady and rapidly changing flow, characterised by rapid changes and sudden changes in flow depth and velocity, and the presence of wetting and drying fronts.

The causes of the dam break problem can be in several orders like technical problems, natural and human causes. The type of technical problems can lead to the collapse of the structure. It could be a malfunction of the valves that allows the flood to discharge or a design, construction or material flaw. The incidence of these problems is influenced by the type of dam, the materials used, the nature of the foundations and the age of the structure. However, modern dams are much safer as a result of developments in construction techniques. The natural causes can be explained by exceptional floods with an intensity higher than that used for the design of the structures, known as the design flood. The safety level adopted is generally between the millennial and decadal floods. Earth dams are not submerged and are therefore more vulnerable to overflow landslides, either of the structure itself or of the land surrounding the reservoir. Finally, earthquakes can cause minor damage (deformations, settlements, cracks, etc.). Finally, accidents can be caused by human factors, inadequate prior studies, insufficient controls, operating errors, lack of supervision and maintenance or acts of malice, sabotage and war.

The flood wave causes enormous damage downstream of the dam, followed by inundation, mixing of water and material from the dam, and extensive erosion of the valley. Three aspects of damage can be recognised: human, economic and environmental. The human aspect, ranging from more or less serious injuries to death by drowning, can be isolated or displaced even after the flood. The economic damage, which also ranges from simple damage to the total destruction and deterioration of homes, businesses, structures (bridges, roads, etc.), livestock, paralysis of public services, etc. Finally, there is the environmental harm, which is numerous. Wildlife is destroyed by the passage of water, and soil is washed away, making it difficult to cultivate land. Dams are also responsible for reducing the distribution of fish and preventing them from migrating freely. Fish passes are designed to mitigate this phenomenon and allow migratory fish to pass. Various types of pollution can be caused by the destruction of factories and other industrial buildings. Technological accidents due to the establishment of companies in the valley (toxic waste, explosions caused by reaction with water, etc.) can occur as a result of the passage of the wave.

The generation of accurate hydrographs for dam breaking has been a major concern since the 10th century. Bazin's proposal may have been the first documented dam break experiment in a channel. This was followed by Rutter's analytical solution of the famous one-dimensional Saint Venart equation for sudden dam break. Su and Barners later extended Rutter's solution to include the effect of different channel cross-sections and proposed a useful power-type equation for the phenomenon, but until recent years very little progress has been made on this problem.

This phenomenon is usually considered a rigorous and evidence-based validation test for numerical models due to the variety of phenomena involved, including violent impacts with and between fluid masses, wave formation and movement, and energy dissipation stages that can be identified before a stable hydrostatic equilibrium is reached. Indeed, it's reasonable to assume that a numerical model that can cope with a dam-break flow will also be able to accurately simulate less severe, slower floods [1, 14, 5, 16].

1.12   Conclusion

This introductory chapter has provided a bibliographical reference to define some of the fluid mechanics concepts. The differences between approaches and methods have been discussed, showing that each shines in its own field, making it difficult to choose which is better than the other. The main notions of this project have been briefly presented and will be further more elaborated in the following chapters.

Numerical Modelling using PFEM

2.1 Introduction

This chapter deals with the numerical tool proposed by Idelsohn and Oñate in their research entitled Particle Finite Element Method, which is the keyword of this project. The aspect of the technique is explained in more detail, starting from its basic characteristics up to the treatment of the incompressible Navier-Stokes equations. For this purpose, the papers published by the distinguished researchers are mainly used.

2.2 Particle Finite Element Method

The Particle Finite Element Method is a powerful numerical analysis and scientific computing tool. It was introduced in the last two decades by Oñate and Idelsohn to deal with problems involving the interaction of fluids and structures, taking into account large fluid free surface motions and the presence of fully or partially submerged bodies. Examples of this type are common in ship hydrodynamics, offshore structures, spillways in dams, free surface channel flows, liquid tanks, agitated reactors, mould filling processes, etc. Later it was applied to a variety of simulation problems such as erosion processes, mixing processes, coupled thermo-viscous processes, thermal diffusion problems and melting of objects in fires. In particular, PFEM is often used to solve fluid-structure interaction problems such as dam-break[22].

PFEM is a particle method in the sense that the domain is defined by a collection of particles that move in a Lagrangian manner, which means that the behaviour of a physical problem is represented by a collection of particles that move according to their own mass and the internal external forces applied to them. All physical and mathematical properties are associated with the particle itself. For example, physical properties such as viscosity or density, physical variables such as velocity, temperature or pressure, and also mathematical variables such as gradients or volumetric deformations are assigned to each particle and represent an average of the property around the particle's position. The interaction forces between particles are evaluated using a mesh, the mesh nodes coincide with the particles so that when the particle moves, so does the mesh. [23]

In PFEM, the governing equations of the Lagrangian framework are solved using the finite element method. Therefore, a mesh that discretises the domain must be generated to solve these governing equations. It should be noted that the mesh nodes discretising the domain can be considered as material particles whose motion is tracked during the transient solution. The quality of the numerical solution will obviously depend on the discretisation chosen, as in standard FEM. The finite element results provide detailed information on pressure, velocity and viscous stress fields.

This method requires a fast regeneration of the mesh at each time step, the Extended Delaunay Tessellation (EDT) is applied to connect the neighbouring particles and allows the generation of non-standard meshes combining arbitrary polyhedric shapes, triangles, quadrilaterals and other polygons in 2D; tetrahedra and arbitrary polyhedrics in 3D, in a computation time of order n, where n is the total number of nodes in the mesh. Typically, the Delaunay triangulation is used, since in 2D it has remarkable properties such as the minimisation of the maximum radius of an element circumcircle, the maximisation of the minimum angle between all elements (max, min propriety). However, the 3D Delaunay algorithm loses some of the optimal properties of its 2D counterpart, which leads to the possible presence of poor quality tetrahedra in the mesh, such as zero volume elements[10].

However, Delaunay tessellation produces a convex figure that does not respect the internal and external physical boundaries, as some boundaries (such as the free surface fluid) may be severely distorted during the solution process, including separation and re-entry of nodes. To detect boundaries, PFEM uses the alpha-shape technique, which is also the simplest way to identify isolated fluid particles outside the main fluid domain. These particles are treated as part of the outer boundary where the pressure is set to atmospheric. The mass lost when a boundary element is eliminated by removing a node from the analysis domain is recovered when the node falls and a new boundary element is created by the alpha shape algorithm. This technique is based on the observation that the non-physical elements that do not belong to the real domain are generally the largest and most distorted because they connect nodes that are far apart. [23, 10, 20].

In short the fundamental features of PFEM are the following:

- Lagrangian framework for the description of motion;

- The mesh nodes where all the information is stored, are treated as physical particles;

- The FEM is used to solve the governing equations;

- Mesh connectivity is regenerated with Delaunay Triangulation;

- Boundaries are recovered through Alpha shape technique.

2.3   The basic steps of PFEM

A typical solution using PFEM can be generalised into a scheme that is used to solve the different types of problems that arise. This scheme is explained in detail in this section. For the sake of clarity, we will define the collection or cloud of nodes (C) corresponding to the fluid and solid domains, the volume (V) defining the analysis domain for the fluid and solid, and the mesh (M) discretising both domains. The following reference [20] is mostly used in this section.

Step 01

The starting point at each time step is the cloud of points in the fluid and solid domains, also referred to as particles, where the mathematical information and physical quantities are stored. For example, C^n denotes the cloud at time t=t_n.

Step 02

Identify the boundaries for both the fluid and solid domains that establish the analysis domain V^n in the fluid and solid. The alpha shape method is used to define the boundaries.

The definition of the alpha shape method is found in[21], which assumes that the nodes follow a variable h(x) distribution, where h(x) is the minimum distance between two particles, all particles on an empty sphere with a radius greater than αh are considered boundary particles. Thus α is a parameter close to, but greater than one, which leads to values of α around 1.3 have been found to be optimal in all examples analysed.

Step 03

The fluid and solid domains are discretised with a finite element mesh M^n. We use an effective mesh generation scheme based on EDT, typically Delaunay triangulation is commonly used.

Given a cloud of N points, the Delaunay triangulation is achieved by constructing the Vernoï diagram, which is defined as the partition of $\mathbb{R}^3$ in convex regions T_i, where each region T_i is associated with a node n_i such that each point of T_i is closer to n_i than to any other node n_j with i $\neq$ j. T_i is also called a Vernoï cell. Each Vernoï cell is convex and closed if it is inside, open if it is at the boundary[10].

The Delaunay triangulation can be constructed by joining the parts whose Vernoï cells have a common boundary, it is also considered the dual of the Vernoï diagram because two nodes of the Delaunay triangulation are joined by an edge only if the respective Vernoï cells share a boundary. A fundamental property of the Delaunay triangulation is that none of its vertices are inside the circumsphere of a tetrahedron (in 3D). Moreover, the vertices of the Vernoï cells represent the centre of the tetrahedron's circumsphere (in 3D) of the triangles circumcircle (in 2D) of the Delaunay triangulation[10].

Step 04

Solve the coupled Lagrangian equations of motion for the overall continuum with the FEM. Compute the state variables in at the next (updated) configuration for t + Δt: velocity, pressure and viscous stresses in the fluid and displacement, stress and strains in the solid. This step will be detailed in the next section.

Step 05

Move the mesh nodes to a new position C^{n+1} where n+1 denotes the time tn+Δt, in terms of time increment size. This step is typically a consequence of the solution process of step 04.

Step 06

Go back to Step 01 and repeat the solution for the next time step to obtain C^{n+2}.

The following figure 2.1, illustrates a sequence of steps to update a "cloud" of nodes representing a domain containing a fluid and a solid part from time n (t = t_n) to time n+2 (t = t_n + 2Δt).
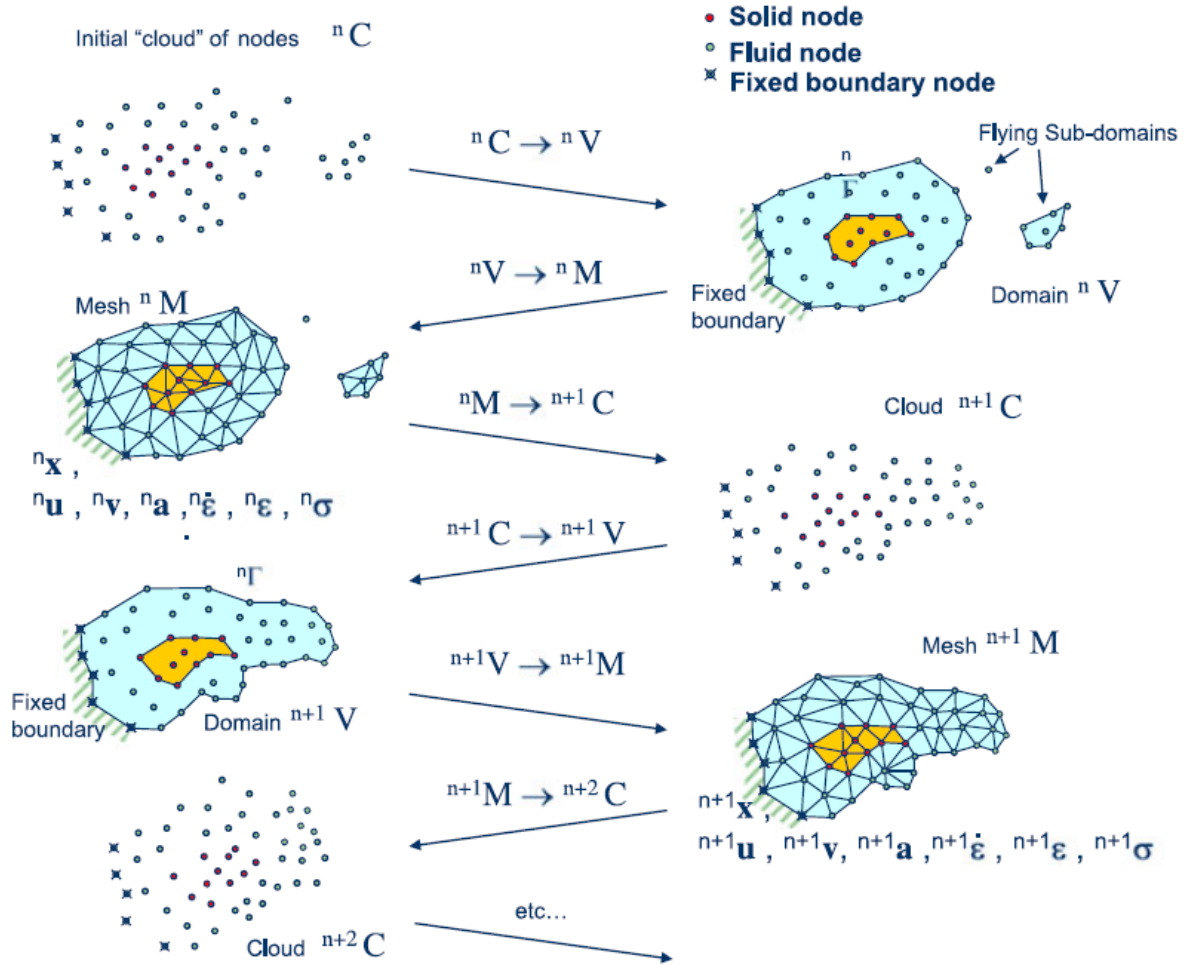
Figure 2.1: PFEM basic steps[20].

2.4   Solving the Lagrangian equations with FEM

As mentioned above, this section details step 04 using the [21, 19] reference. The latter implies that the particle positions are updated by solving the Lagrangian form of the Navier-Stokes equations.

2.4.1   Governing Lagrangian equations in a viscous fluid flow

PFEM solves the fluid mechanics equations in a Lagrangian way. Mass Conservation and Momentum Conservation equations (Navier-Stokes) are written the following way, where (i and j) are dummy indices:

Mass conservation:

$$\frac{D\rho}{Dt} = -\rho \frac{\partial u_i}{\partial x_i} \tag{2.1}$$

19

Momentum conservation:

$$\rho \frac{Du_i}{Dt} = -\frac{\partial}{\partial x_i} P + \frac{\partial}{\partial x_j} \tau_{ij} + \rho f_i \tag{2.2}$$

For Newtonian fluids the stress tensor τ_{ij} may be expressed as a function of the velocity field through the viscosity μ by

$$\tau_{ij} = \mu \left(\frac{\partial u_i}{\partial x_j} + \frac{\partial u_j}{\partial x_i} - \frac{2}{3} \frac{\partial u_l}{\partial x_l} \delta_{ij} \right) \tag{2.3}$$

For near incompressible flows $\partial u_i \, / \, \partial x_i \ll \partial u_k \, / \, \partial x_l$ the term

$$\frac{2\mu}{3} \frac{\partial u_l}{\partial x_l} \approx 0 \tag{2.4}$$

and it may be neglected in 2.3. Then

$$\tau_{ij} \approx \mu \left(\frac{\partial u_i}{\partial x_j} + \frac{\partial u_j}{\partial x_i} \right) \tag{2.5}$$

In the same way, the term $(\partial/\partial x_j)\tau_{ij}$ in the momentum equations may be simplified for near incompressible flows as

$$\frac{\partial}{\partial x_j} \tau_{ij} = \frac{\partial}{\partial x_j} \left(\mu \left(\frac{\partial u_i}{\partial x_j} + \frac{\partial u_j}{\partial x_i} \right) \right) = \mu \frac{\partial}{\partial x_j} \left(\frac{\partial u_i}{\partial x_j} \right) + \mu \frac{\partial}{\partial x_j} \left(\frac{\partial u_j}{\partial x_i} \right)$$

$$= \mu \frac{\partial}{\partial x_j} \left(\frac{\partial u_i}{\partial x_j} \right) + \mu \frac{\partial}{\partial x_i} \left(\frac{\partial u_j}{\partial x_j} \right) \approx \mu \frac{\partial}{\partial x_j} \frac{\partial u_i}{\partial x_j} \tag{2.6}$$

Then, the momentum equations can be finally written as:

$$\rho \frac{Du_i}{Dt} = -\frac{\partial}{\partial x_i} P + \frac{\partial}{\partial x_j} \tau_{ij} + \rho f_i \approx -\frac{\partial}{\partial x_i} P + \mu \frac{\partial}{\partial x_j} \left(\frac{\partial u_i}{\partial x_j} \right) + \rho f_i \tag{2.7}$$

Boundary conditions

On the boundaries, the standard boundary conditions for the Navier–Stokes equations are:

$$\tau_{ij} v_j - P v_i = \bar{\sigma} \quad on \;\; \Gamma_\sigma$$

$$u_i v_i = \bar{u}_n \quad on \;\; \Gamma_n$$

$$u_i \zeta_i = \bar{u}_t \quad on \;\; \Gamma_t$$

Where v_i and ζ_i are the components of the normal and tangent vector to the boundary.

2.4.2   Implicit time integration

The momentum equation 2.7 will be integrated implicitly in time as:

$$\rho\frac{Du_i}{Dt} \approx \rho\frac{u_i^{n+1} - u_i^n}{\Delta t} = \left[-\frac{\partial}{\partial x_i}P + \mu\frac{\partial}{\partial x_j}\left(\frac{\partial u_i}{\partial x_j}\right) + \rho f_i\right]^{n+1}$$

$$= \left[-\frac{\partial}{\partial x_i}P\right]^{n+1} + \left[\mu\frac{\partial}{\partial x_j}\left(\frac{\partial u_i}{\partial x_j}\right) + \rho f_i\right]^{n+1} \tag{2.8}$$

The mass conservation 2.1 is also integrated implicitly by:

$$\frac{D\rho}{Dt} \approx \frac{\rho^{n+1} - \rho^n}{\Delta t} = \left[-\rho\frac{\partial(u_i)}{\partial x_i}\right]^{n+1} = -\rho^{n+1}\frac{\partial u_i^{n+1}}{\partial x_i} \tag{2.9}$$

2.4.3   The time splitting

According to [21], due to the fully coupled equation with four degrees of freedom per node, the time integration of equation 2.8 presents some difficulties. In the case of an incompressible or nearly incompressible fluid, the fact that the three components of velocity in equation 2.8 are coupled only through pressure can be advantageous. The fractional step method proposed in [9] is used, which consists in dividing each time step into two pseudo time steps. In this paper, the results are presented directly with fixed parameters, indicating a fully implicit integration and a large pressure split, resulting in better pressure stabilisation. The fractional-step algorithm for equations 2.8 and 2.9 is the following:

Split of the momentum equations

$$\frac{Du_i}{Dt} \approx \frac{u_i^{n+1} - u_i^n}{\Delta t} = \frac{u_i^{n+1} - u_i^* + u_i^* - u_i^n}{\Delta t} = -\frac{1}{\rho}\frac{\partial}{\partial x_i}P^{n+1} + \frac{1}{\rho}\mu\frac{\partial}{\partial x_j}\frac{\partial u_i^{n+1}}{\partial x_j} + f_i \tag{2.10}$$

Where u_i^* are fictitious variables termed fractional velocities defined by the split:

$$\frac{u_i^* - u_i^n}{\Delta t} = \frac{1}{\rho}\mu\frac{\partial}{\partial x_j}\frac{\partial u_i^{n+1}}{\partial x_j} + f_i \tag{2.11a}$$

$$\frac{u_i^{n+1} - u_i^*}{\Delta t} = -\frac{1}{\rho}\frac{\partial}{\partial x_i}P^{n+1} \tag{2.11b}$$

With the use of the time fraction in [9] and putting the proper values of the parameters, the following approximation is found:

$$\mu\frac{\partial}{\partial x_j}\left(\frac{\partial u_i^{n+1}}{\partial x_j}\right) \approx \mu\frac{\partial}{\partial x_j}\left(\frac{\partial u_i^*}{\partial x_j}\right) \tag{2.12}$$

Taking into account equation 2.12, 2.11a may be written as:

$$(A) \qquad u_i^* - \frac{\Delta t}{\rho} \mu \frac{\partial}{\partial x_j} \left(\frac{\partial u_i^*}{\partial x_j} \right) = u_i^n + f_i \Delta t \tag{2.13}$$

Also 2.11b is written as follow:

$$(C) \qquad u_i^{n+1} = u_i^* - \frac{\Delta t}{\rho} \frac{\partial}{\partial x_i} P^{n+1} \tag{2.14}$$

Split of the mass conservation equations

$$\frac{D\rho}{Dt} \approx \frac{\rho^{n+1} - \rho^n}{\Delta t} = \frac{\rho^{n+1} - \rho^* + \rho^* - \rho^n}{\Delta t} = -\rho \frac{\partial (u_i^{n+1} - u_i^* + u_i^*)}{\partial x_i} \tag{2.15}$$

where ρ^* is a fictitious variable defined by the split

$$\frac{\rho^* - \rho^n}{\Delta t} = -\rho \frac{\partial u_i^*}{\partial x_i} \tag{2.16a}$$

$$\frac{\rho^{n+1} - \rho^*}{\Delta t} = -\rho \frac{\partial (u_i^{n+1} - u_i^*)}{\partial x_i} \tag{2.16b}$$

Coupled equations

From equations 2.14 and 2.16 the coupled mass–momentum equation becomes

$$\frac{\rho^{n+1} - \rho^*}{\Delta t^2} = \frac{\partial^2}{\partial x^2} (P^{n+1}) \tag{2.17}$$

Taking into account equation 2.16a, the above expression can be written as

$$\frac{\rho^{n+1} - \rho^n}{\Delta t^2} + \frac{\rho}{\Delta t} \frac{\partial u_i^*}{\partial x_i} = \frac{\partial^2}{\partial x_i^2} (P^{n+1}) \tag{2.18}$$

In equation 2.18 the incompressibility condition has not been introduced yet. The simplest way to introduce the incompressibility condition in a Lagrangian formulation is to write

$$\rho^{n+1} = \rho^n = \rho^0 = \rho \tag{2.19}$$

Then, the first term of equation 2.18 disappears, giving

$$(B) \qquad \frac{\rho}{\Delta t} \frac{\partial u_i^*}{\partial x_i} = \frac{\partial^2}{\partial x_i^2} (P^{n+1}) \tag{2.20}$$

The three step fractional method used here can be summarised by:

$$(A) \qquad u_i^* - \frac{\Delta t}{\rho}\mu\frac{\partial}{\partial x_j}\left(\frac{\partial u_i^*}{\partial x_j}\right) = u_i^n + f_i\Delta t \qquad \Rightarrow u_i^* \qquad (2.21)$$

$$(B) \qquad \frac{\rho}{\Delta t}\frac{\partial u_i^*}{\partial x_i} = \frac{\partial^2}{\partial x_i^2}(P^{n+1}) \qquad \Rightarrow P^{n+1} \qquad (2.22)$$

$$(C) \qquad u_i^{n+1} = u_i^* - \frac{\Delta t}{\rho}\frac{\partial}{\partial x_i}(P^{n+1}) \qquad \Rightarrow u^{n+1} \qquad (2.23)$$

2.4.4　Generation of new mesh

One of the keys to the success of the Lagrangian flow formulation described above is the rapid regeneration of the mesh at any time, based on the location of the nodes in the space domain. As already mentioned, this is done using the EDT described above. An original aspect of the Lagrangian formulation is the combination of different geometric elements within the same mesh.

Once the new mesh has been generated at each time step, the numerical solution is found using the finite element algorithm described in the next subsection.

2.4.5　Spatial discretization via the Meshless Finite Element Method

The unknown functions are approximated using an equal order interpolation for all variables in the final configuration in a general 1D case

$$u_i = \sum_l N_l(x,t)U_{il}$$

$$p = \sum_l N_l(x,t)P_l$$

In matrix form

$$u_i = N^T(x,t)U_i$$

$$p = N^T(x,t)P \qquad (2.24)$$

or in compact form

$$u_i = N_i^T U = \begin{bmatrix} N^T & & \\ & N^T & \\ & & N^T \end{bmatrix} U \qquad (2.25)$$

Where N^T are the MFEM shape functions and U, P the nodal values of the three components of the unknown velocity and the pressure, respectively.

It must be noted that the shape functions N(x,t) are functions of the particle co-ordinates. Then, the shape functions may change in time following the particles position. During the time step a mesh update may introduce change in the shape function definition which must be taken into account. During the time integration there are two times involved: t^n and t^{n+1}. The following notation will be used to distinguish between N(x, t^n) and N(x, t^{n+1}):

$$N(x, t^n) = N^n \quad and \quad N(x, t^{n+1}) = N^{n+1} \tag{2.26}$$

Using the Galerkin weighted residual method to solve the split equations 2.21, 2.22 and 2.23 the following integrals must be written:

$$(A) \quad \int_V N_i \left[u_i^* - \frac{\Delta t}{\rho} \mu \frac{\partial}{\partial x_j} \left(\frac{\partial u_i^*}{\partial x_j} \right) - u_i^n - \Delta t f_i \right] dV$$

$$- \frac{\Delta t}{\rho} \int_{\Gamma_\sigma} N_i \left(\bar{\sigma}_{ni} - \left(\tau_{ij}^{n+1} v_j - \gamma P^n v_i \right) \right) d\Gamma = 0 \tag{2.27}$$

$$(B) \quad \int_V N \left[\frac{\rho}{\Delta t} \frac{\partial u_i^*}{\partial x_i} - \frac{\partial^2}{\partial x_i} P^{n+1} \right] dV$$

$$- \frac{\rho}{\Delta t} \int_{\Gamma_u} N \left(u_i^{n+1} v_i - \bar{u}_i^{n+1} v_i \right) d\Gamma = 0 \tag{2.28}$$

$$(C) \quad \int_V N_i \left[u_i^{n+1} - u_i^* + \frac{\Delta t}{\rho} \frac{\partial}{\partial x_i} P^{n+1} \right] dV$$

$$- \int_{\Gamma_\sigma} N_i \left(P^{n+1} v_i - \gamma \widehat{P}^n v_i \right) d\Gamma = 0 \tag{2.29}$$

The last term in the equations above, represent the boundary conditions, where they have also been split and V is the volume at time t^{n+1}. Integrating by part some of the terms, noting that the essential and natural boundary conditions of equation 2.28 are:

$$P = 0 \quad on \quad \Gamma_\phi$$

$$\bar{u}^{n+1} v = 0 \quad on \quad \Gamma_u$$

The previous equations become:

$$(A) \quad \int_V N_i u_i^* dV - \frac{\Delta t}{\rho} \mu \int_V \frac{\partial N_i}{\partial x_j} \left(\frac{\partial u_i^*}{\partial x_j} \right) dV$$

$$- \int_V N_i u_i^n dV - \Delta t \int_V N_i f_i dV - \frac{\Delta t}{\rho} \int_{\Gamma_\sigma} N_i \bar{\sigma}_{ni} d\Gamma = 0 \tag{2.30}$$

$$(B) \quad \frac{\rho}{\Delta t}\int_V \frac{\partial N}{\partial x_i}u_i^* - \int_V \frac{\partial N}{\partial x_i}\frac{\partial}{\partial x_i}P^{n+1} - \int_{\Gamma_u} N\bar{u}_i^{n+1}d\Gamma = 0 \tag{2.31}$$

$$(C) \quad \int_V N_i u_i^{n+1}dV - \int_V N_i u_i^* dV + \frac{\Delta t}{\rho}\int_V N_i \frac{\partial}{\partial x_i}P^{n+1}dV = 0 \tag{2.32}$$

Discrete equations. Using approximations 2.24 and 2.26 the discrete equations become:

$$(A) \quad \int_V N_i N_i^T dV u_i^* - \frac{\Delta t}{\rho}\mu \int_V \frac{\partial N_i}{\partial x_j}\frac{\partial N_i^T}{\partial x_j}dV u_i^*$$

$$= \int_V N_i N_i^T dV u_i^n + \Delta t \int_V N_i f_i dV + \frac{\Delta t}{\rho}\int_{\Gamma_\sigma} N_i \bar{\sigma}_{ni}d\Gamma \tag{2.33}$$

In compact form:

$$(A) \quad \left(M - \frac{\delta}{\rho}\mu K\right)U^* = MU_i^n + \Delta t F \tag{2.34}$$

In the same way:

$$(B) \quad \frac{\partial N_i}{\partial x_i}\frac{\partial N_i^T}{\partial x_i}dV P^{n+1} = \frac{\rho}{\Delta t}\int_V \frac{\partial N_i}{\partial x_i}N_i^T dV u_i^* - \frac{\rho}{\Delta t}\int_{\Gamma_u} N\bar{u}_i^{n+1}d\Gamma \tag{2.35}$$

In compact form:

$$(B) \quad SP^{n+1} = \frac{\rho}{\Delta t}\left(BU^* - \hat{U}\right) \tag{2.36}$$

Finally:

$$(C) \quad \int_V N_i N_i^T dV u_i^{n+1} = \int_V N_i N_i^T dV u_i^* - \frac{\Delta t}{\rho}\int_V N_i \frac{\partial N_i^T}{\partial x_i}dV P^{n+1} \tag{2.37}$$

In compact form:

$$(C) \quad MU^{n+1} = MU^* - \frac{\Delta t}{\rho}B^T P^{n+1} \tag{2.38}$$

where the matrices are

$$M = \begin{bmatrix} M_p & 0 & 0 \\ 0 & M_p & 0 \\ 0 & 0 & M_p \end{bmatrix} \tag{2.39}$$

$$M_p = \int_V N N^T dV \tag{2.40}$$

$$B = \left[\int_V \left(\frac{\partial N}{\partial x}N^T\right)dV ; \int_V \left(\frac{\partial N}{\partial y}N^T\right)dV ; \int_V \left(\frac{\partial N}{\partial z}N^T\right)dV\right] \tag{2.41}$$

$$S = \int_V \left(\frac{\partial N}{\partial x}\frac{\partial N^T}{\partial x} + \frac{\partial N}{\partial y}\frac{\partial N^T}{\partial y} + \frac{\partial N}{\partial z}\frac{\partial N^T}{\partial z}\right)dV \tag{2.42}$$

$$\widehat{U} = \int_{\Gamma_u} N \bar{u}_i^{n+1} d\Gamma \tag{2.43}$$

$$K = \begin{bmatrix} S & 0 & 0 \\ 0 & S & 0 \\ 0 & 0 & S \end{bmatrix} \tag{2.44}$$

$$F^T = \left[\int_V f_x dV ; \int_V N^T f_y dV ; \int_V N^T f_z dV \right]$$

$$+ \frac{1}{\rho} \left[\int_{\Gamma_\sigma} N^T \bar{\sigma}_{nx} d\Gamma ; \int_{\Gamma_\sigma} N^T \bar{\sigma}_{ny} d\Gamma ; \int_{\Gamma_\sigma} N^T \bar{\sigma}_{nz} d\Gamma \right] \tag{2.45}$$

2.4.6   Summary of a full iterative time step

The full step can be described as follows: beginning with known values of u^n and P^n in each particle, with an approximate value of $u^{n+1} = 0$. The particles will then move to a new position of x^{n+1} and generate a new mesh. Next, the velocities u^* and P^{n+1} are evaluated from 2.34 and 2.36 respectively, which will lead to the evaluation of the velocity u^{n+1} 2.38, the value that will be used again to repeat the until process until it converges. The following steps are better visualised in the following schema:
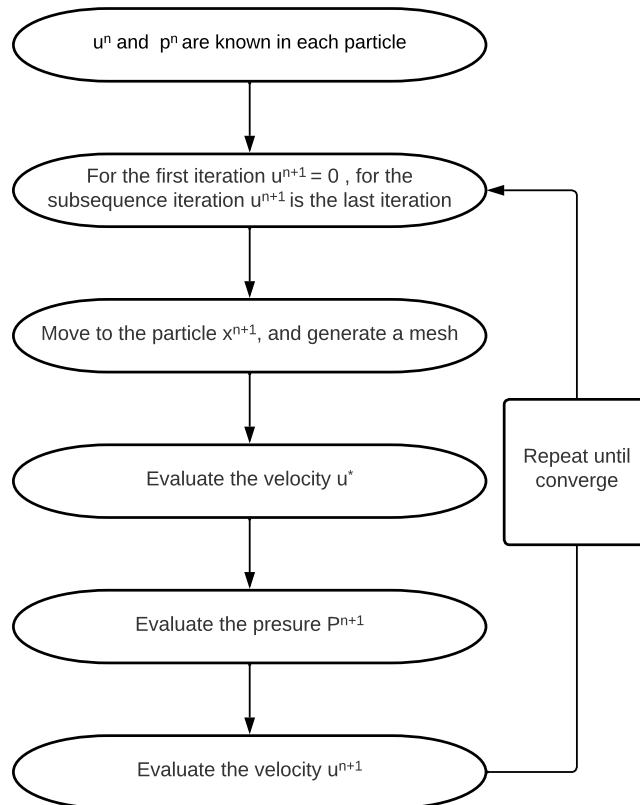

Figure 2.2: Representative scheme of the full iterative time step.

2.5   Conclusion

The numerical technique, Particle Finite Element Method, is discussed in this chapter from an overview of its features to the way it solves the Lagrangian form of the incompressible Navier-Stokes equations. The numerical method is also the main subject of this project and will be used in the numerical modelling of the two dam break experiences presented in the upcoming chapters.

Beam Element Modelling

3.1 Introduction

In the following chapter, a detailed numerical modelling about the elastic obstacle in the dam-break numerical experiment, which a finite element analysis for a 2D beam. To write this one, the course of [40] previously seen is used as a reference.

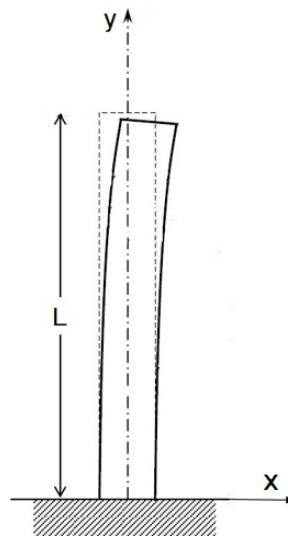## 3.2 Beam Element in FEM

3.2.1 Governing equation

Figure 3.1: Vertical Beam

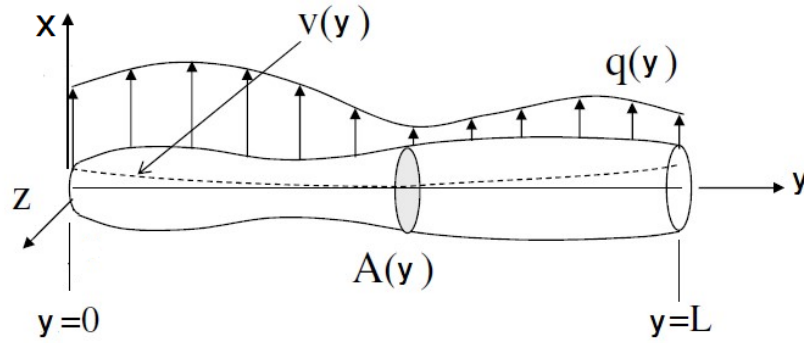Figure 3.2: Beam

Beam of length L, with variable longitudinal section (A(y)), subjected to a longitudinal load (q(y) in the x-direction) with longitudinal displacement (v(y) in the x-direction). It is assumed that the vertical section remains flat and perpendicular after the deformation; they therefore undergo a small angle of rotation θ in the (oxy)plane. Due to this rotation, the points of the vertical section experience a vertical displacement u, which varies vertically from the lower fibre to the upper fibre, which is worth:

$$u = -x\theta = -x\frac{\partial v}{\partial y} \tag{3.1}$$

x: the distance from the middle line (centre of the section)

The stress distribution along the section is given by Hooke's Law:

$$\sigma_y = E\varepsilon_y = E\frac{\partial u}{\partial y} = -Ex\frac{\partial^2 v}{\partial y^2} \tag{3.2}$$

E: the modulus of elasticity of material of the beam;
ε_y: the axial strain in the y-direction along the section, after assuming small strain.

The moment produced by the external load M must be balanced by the moment produced by these stresses:

$$M - \int_s \sigma x ds = 0$$

$$M = E\frac{\partial^2 v}{\partial y^2}\int_s x^2 ds \tag{3.3}$$

s: the area of the cross-section.

Let I_z be the moment of inertia with respect to the z axis perpendicular to the plane (xy):

$$I = \int_s x^2 ds$$

29

The Moment expression becomes:

$$M = EI \frac{\partial^2 v}{\partial y^2} \tag{3.4}$$

Considering the static equilibrium of an element dy:
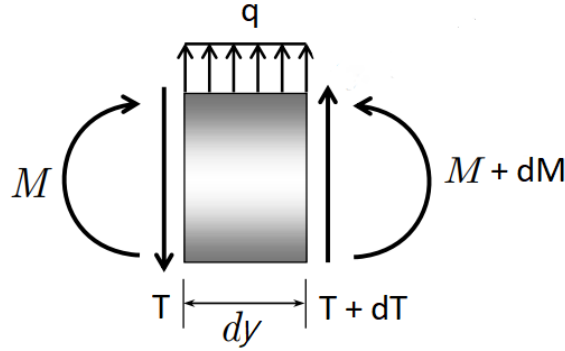

Figure 3.3: Static equilibrium

The sum of the moments with respect to the centre of gravity gives:

$$-M + T\frac{dy}{2} + (T + dT)\frac{dy}{2} + (M + dM) = 0 \tag{3.5}$$

Neglecting $T\frac{dy}{2}$, the relation between the Shear force and the bending moment is obtained:

$$T = -\frac{dM}{dy} = -\frac{\partial}{\partial y}\left(EI\frac{\partial^2 v}{\partial y^2}\right) \tag{3.6}$$

Equilibrium of horizontal forces for positive loading along the x-axis, gives the relationship between load q and shear force and relates the load to the displacement v:

$$T + dT + qdy - T = 0 \tag{3.7}$$

$$q = -\frac{dT}{dy} = \frac{\partial^2}{\partial y^2}\left(EI\frac{\partial^2 v}{\partial y^2}\right) \tag{3.8}$$

This equation translates the static equilibrium of the beam. In the case of a dynamic movement, it is necessary to add a term in 3.7 which translates the force of inertia:

$$F_i = m\gamma = \rho A dy \frac{\partial^2 u}{\partial t^2} \tag{3.9}$$

ρ : the density of the material;
A : Beam section;
t : time.

Equation 3.7 becomes the Euler-Bernoulli equation for the bending of a beam:

$$T + dT + qdy - T = F_i \tag{3.10}$$

Equation 3.8 becomes 3.11, where the displacement v is a function of the y coordinate along the beam axis and the time t:

$$\rho A \frac{\partial^2 v}{\partial t^2} + \frac{\partial^2}{\partial y^2}(EI\frac{\partial^2 v}{\partial y^2}) = q(y) \tag{3.11}$$

3.2.2   Formulation of the element

Variational formulation

The strong variational formulation associated with 3.11 is written:

$$\int_0^L \delta v \rho A \frac{\partial^2 v}{\partial t^2} dy + \int_0^L \delta v \frac{\partial^2}{\partial y^2}(EI\frac{\partial^2 v}{\partial y^2}) dy = \int_0^L \delta v q(y) dy \tag{3.12}$$

L: the length of beam;
δv: weight function.

Two integration's by parts of the second term give the weak integral form:

$$\int_0^L \delta v \rho A \frac{\partial^2 v}{\partial t^2} dy + \int_0^L \frac{\partial^2 \delta v}{\partial y^2} EI \frac{\partial^2 v}{\partial y^2} dy + \left[\delta v \frac{\partial}{\partial y}(EI\frac{\partial^2 v}{\partial y^2})\right]_0^L + \left[\frac{\partial \delta v}{\partial y}(EI\frac{\partial^2 v}{\partial y^2})\right]_0^L = \int_0^L \delta v q(y) dy \tag{3.13}$$

The derivative of the disturbances of displacements is replaced by a disturbance of rotation, the boundary conditions are written as follows:

$$\left[\frac{\partial \delta v}{\partial y}(EI\frac{\partial^2 v}{\partial y^2})\right]_0^L = \delta\theta\Big\|_{y=L} M_L - \delta\theta\Big\|_{y=0} M_0$$

$$\left[\delta v \frac{\partial}{\partial y}(EI\frac{\partial^2 v}{\partial y^2})\right]_0^L = \delta v\Big\|_{y=L} T_L - \delta v\Big\|_{y=0} T_0$$

The final expression of weak form:

$$\int_0^L \delta v \rho A \frac{\partial^2 v}{\partial t^2} dy + \int_0^L \frac{\partial^2 \delta v}{\partial y^2} EI \frac{\partial^2 v}{\partial y^2} dy + \delta\theta\Big\|_{y=L} M_L +$$

$$\delta v\Big\|_{y=L} T_L - \delta\theta\Big\|_{y=0} M_0 - \delta v\Big\|_{y=0} T_0 = \int_0^L \delta v q(y) dy \tag{3.14}$$
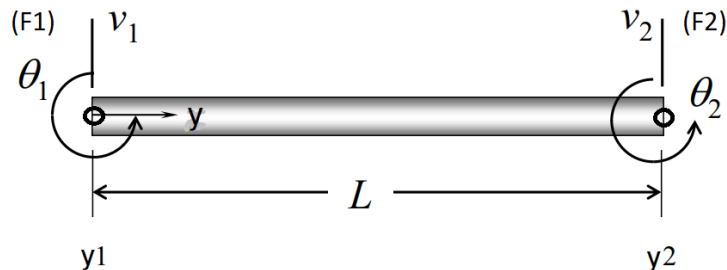
Discretisation

Figure 3.4: Two-node beam element

For the discretisation of the equation of weak form, an element with two nodes is considered, where concentrated forces and couples can only be applied. The use of two degrees of freedom, because of the expression of the constraints, on the boundaries involves rotation, thus guaranteeing the continuity of the displacement and its derivatives, i.e. the rotations. The number of DOF reaches four and the interpolation polynomial has to be cubic (four constants).

The vector of elementary displacements and rotations is therefore written as follows:

$$u_n = \begin{pmatrix} v_1 & \theta_1 & v_2 & \theta_2 \end{pmatrix}^T \tag{3.15}$$

Displacements and rotations along the beam are approximated by:

$$v(y) = a_0 + a_1 y + a_2 y^2 + a_3 y^3 \tag{3.16a}$$

$$\theta(y) = a_1 + 2a_2 y + 3a_3 y^2 \tag{3.16b}$$

The evaluation of these polynomials at the nodes gives:

$$v(0) = a_0 = v_1 \tag{3.17a}$$

$$\theta(0) = a_1 = \theta_1 \tag{3.17b}$$

$$v(L) = v_2 = v_1 + \theta_1 L + a_2 L^2 + a_3 L^3 \tag{3.18a}$$

$$\theta(L) = \theta_2 = \theta_1 + 2a_2 L + 3a_3 L^2 \tag{3.18b}$$

The resolution of the equations 3.18 for a_2 and a_3 gives:

$$a_2 = \frac{3}{L^2}(v_2 - v_1) - \frac{1}{L}(2\theta_1 + \theta_2) \tag{3.19a}$$

$$a_3 = \frac{2}{L^3}(v_1 - v_2) + \frac{1}{L^2}(\theta_2 + \theta_1) \tag{3.19b}$$

By replacing these parameters in 3.16 and after arrangement of the terms, the nodal interpolation of the displacements are written in the form:

$$v(y) = [N_1(y) + N_2(y) + N_3(y) + N_4(y)] \begin{Bmatrix} v_1 \\ \theta_1 \\ v_2 \\ \theta_2 \end{Bmatrix} \tag{3.20}$$

The shape functions N_i are called Hermite polynomials, their expression are:

$$\begin{cases} N_1 = 1 - \dfrac{3y^2}{L^2} & \text{(3.21a)} \\[2mm] N_2 = x - \dfrac{2y^2}{L} + \dfrac{y^3}{L^2} & \text{(3.21b)} \\[2mm] N_3 = \dfrac{3y^2}{L^2} - \dfrac{2y^3}{L^3} & \text{(3.21c)} \\[2mm] N_4 = \dfrac{y^3}{L^2} - \dfrac{y^2}{L} & \text{(3.21d)} \end{cases}$$

Elementary matrices

Replacing the displacement v in the variational form of 3.14 by its approximation in 3.20, gives the following for the perturbations:

$$\delta v = \delta u_n^T N^T \tag{3.22a}$$

$$\delta \theta = \delta u_n^T \frac{dN^T}{dy} \tag{3.22b}$$

$$\delta u_n^T = (\delta v_1 \quad \delta \theta_1 \quad \delta v_2 \quad \delta \theta_2) \tag{3.22c}$$

The derivation become:

$$\frac{\partial^2 v}{\partial y^2} = \frac{d^2 N}{dy^2} u_n \tag{3.23a}$$

$$\frac{\partial^2 v}{\partial t^2} = N \frac{d^2 u_n}{dt^2} = N \ddot{u}_n \tag{3.23b}$$

$$\frac{d^2 N}{dy^2} = \frac{1}{L^3} (12y - 6L, \quad 6Ly - 4L^2, \quad 6L^2 - 12y, \quad 6Ly - 2L^2) \tag{3.23c}$$

Given the values of the functions N and dN at the nodes, the boundary conditions are written:

$$\delta\theta\Big\|_{y=L} M_L - \delta\theta\Big\|_{y=0} M_o = \left\{(0\ 0\ 0\ 1)^T M_L - (0\ 1\ 0\ 0)^T M_0\right\} = \delta u_n^T (0\ -M_0\ 0\ M_L)^T$$

(3.24a)

$$\delta v\Big\|_{y=L} T_L - \delta v\Big\|_{y=0} T_0 = \left\{(0\ 0\ 1\ 0)^T T_L - (1\ 0\ 0\ 0)^T T_0\right\} = \delta u_n^T (-T_0\ 0\ T_L\ 0)^T \quad (3.24b)$$

The conditions correspond to the external load applied to the nodes. The elementary vector F_n of the forces and moments concentrated at the nodes is written as follows:

$$F_n = (-T_0\ -M_0\ T_L\ M_0)^T \tag{3.24c}$$

The loading F_e distributed on the element beam corresponds to the second term of the form variational 3.14:

$$\int_0^L \delta v q(y)dy = \delta u_n^T \int_0^T N^T q(y)dy$$

$$F_e = \int_0^L N^T q(y)dy \tag{3.25}$$

This load is a function of the distribution q(y). In simple cases we can integrate and give the explicit expression of F_e, otherwise it is possible to subdivide the beam (or element) into several small element so as to replace the load distributed by two equivalent forces concentrated at the extremities.

The expression of F_e is given below for a case of trapezoidal loading varying form q_0 to q_L. The uniform and triangular loads are only special cases of trapezoidal loading.

$$q(y) = q_0 + (q_L - q_0)\frac{y}{L} \tag{3.26}$$

$$F_e = \frac{L}{60}[(9q_L + 21q_0), L(2q_l + 3q_0), (21q_L + 9q_0), -L(3q_L + 2q_0)]^T \tag{3.27}$$

There are now two integral terms in 3.14 to be discretised:

$$\int_0^L \frac{\partial^2 \delta v}{\partial y^2} EI \frac{\partial^2 v}{\partial y^2} dy = \int_0^L \delta u_n^T \frac{d^2 N^T}{dy^2} EI \frac{d^2 N}{dy^2} EI \frac{d^2 N}{dy^2} u_n^T dy \tag{3.28a}$$

$$\int_0^L \delta v \rho A \frac{\partial^2 v}{\partial t^2} dy = \int_0^L \delta u_n^T N^T \rho N \ddot{u}_n dy \tag{3.28b}$$

Eliminating δu_n^T of the discrete integral equation gives the two mass matrices K_e and the stiffness M_e:

$$K_e = \int_0^L \frac{d^2 N^T}{dy^2} EI \frac{d^2 N}{dy^2} dy \tag{3.29a}$$

$$M_e = \int_0^L N^T \rho A N dy \tag{3.29b}$$

If the beam is made of the same homogeneous material and of the same longitudinal section (E, I, A and ρ are constant), then the explicit expression of the elementary matrices can be obtained and are written as follows:

$$K_e = \frac{EI}{L^3} \begin{bmatrix} 12 & 6L & -12 & 6L \\ 6L & 4L^2 & -6L & 2L^2 \\ -12 & -6L & 12 & -6L \\ 6L & 2L^2 & -6L & 4L^2 \end{bmatrix} \tag{3.30a}$$

$$M_e = \frac{\rho A L}{420} \begin{bmatrix} 156 & 22L & 54 & -13L \\ 22L & 4L^2 & 13L & -3L^2 \\ 54 & 13L & 156 & -22L \\ -13L & -3L^2 & -22L & 4L^2 \end{bmatrix} \tag{3.30b}$$

3.3   Conclusion

In this chapter, the numerical analysis of the beam element using the finite element method is detailed, starting from the formulation of the governing equation to obtaining the mass and stiffness matrices. The beam, as mentioned earlier, is the elastic obstacle of the dam-break numerical experimental that will be presented in the next chapter.

Numerical Simulation

4.1   Introduction

This chapter deals with the numerical simulations, where the PFEM is put into practice and two examples of the dam break analysis against obstacle are treated. In the first example, the obstacle is assumed to be rigid and no fluid-structure interaction is considered, only the fluid domain is modelled and the flow is simulated with the impact on the obstacle. In the second example, the assumption of rigidity is dropped and the obstacle is considered to be elastic and deformable. The elastic, bending behaviour under the effect of the fluid flow is modelled using a 2D beam element. The deformation deformations of the obstacle also effect and modify the flow, in this case the fully coupled fluid-structure problems is solved at each time step of the simulation. The results are presented in terms of the fluid shape, the hydrodynamic pressures on the obstacle, the beam deflections, and the flow velocities. All these quantities are evaluated and reported using OpenSeesPy scripting, ParaView visualisation, and Excel plotting tools.

4.2   Dam-break with rigid obstacle

The first numerical application treats the collapse of a water column against a rigid obstacle. The simulations were carried out using a deformable mesh with an alpha shape parameter set to $\alpha = 1.4$ and an average cell size of $h = 5\ mm$. An adaptive time step between 10^{-6} and 10^{-3} was used for the time integration scheme, and the total duration of the analysis is $2\ s$.

This case consists of a rectangular tank of length $L_c = 614\ mm$ and width $H_c = 300\ mm$, in the centre of which a rigid obstacle of length $H_r = 48\ mm$ and width $L_r = 24\ mm$ is placed. A column of water of height $H_f = 292\ mm$ and width $L_f = 146\ mm$ is first positioned between the left wall of the tank and a hypothetical retaining wall. The density of the water and its dynamic viscosity are $\rho_f = 1000\ kg/m^3$ and $\mu = 0.001\ Pa.s$, at the instant $t = 0\ s$ the pressure and the velocity of the fluid are fixed at $P_0 = 0\ Pa$ and $u_0 = 0\ m/s$.

This geometry is a common dam break problem that has been extensively studied (see e.g. [4, 13, 17, 29, 45]). The laboratory experiment will be carried out by [45], which will serve to compare and verify the numerical modelling presented in this paper.
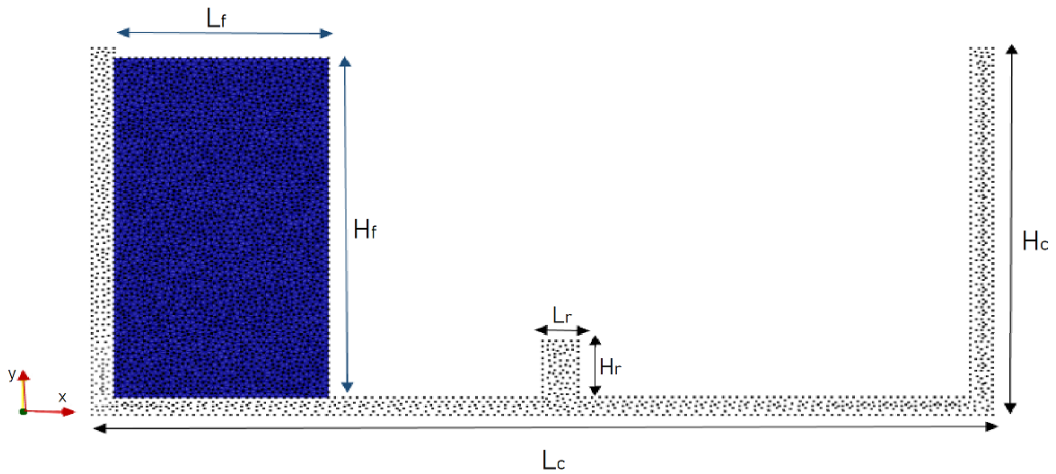

Figure 4.1: Collapse of a water column on a rigid object. Initial geometry of the problem.

Figure 4.2, displays snapshots of the first simulation case of the dam break problem with a rigid obstacle at different time steps corresponding to $t = 0.095\ s$; $t = 0.15\ s$; $t = 0.25\ s$; $t = 0.35\ s$; $t = 0.45\ s$; $t = 1.5\ s$; $t = 1.75\ s$ and $t = 2\ s$, using a refined mesh.

The water initially collapses under gravity after removing the supporting wall and propagates along the channel, as shown at $t = 0.095\ s$, until it reaches the rigid obstacle, then the water begins to rise at this vertical obstacle at $t = 0.15\ s$, this effect is variously referred to as wave action in many articles such as [29]. This wave rises and a narrow curved tongue of water is formed and deflects away from the obstacle, the continued increase in the course results in surface tension causing the formation and detachment of drops at $t = 0.25\ s$. At $t = 0.35\ s$, the tongue of water reaches the right wall of the container and, on contact with it, the water begins to fall under the effect of gravity, trapping air underneath which resists the downward fall, according to the simulation shown in figure 4.2e at instant $t = 0.45\ s$. The water then fills the tank, sloshing between its two walls and submerging the obstacle, as shown in the last three pictures 4.2f, 4.2g and 4.2h (at the times $t = 1.5\ s$; $t = 1.75\ s$ and $t = 2\ s$). At the end of the simulation, the sloshing slows down and the water level starts to stabilise at a fixed level of H_{ff}, which is theoretically calculated to be $H_{ff} = 76.13\ mm$.

(a) $t = 0.095\ s$

(b) $t = 0.15\ s$

(c) $t = 0.25\ s$

(d) $t = 0.35\ s$

(e) $t = 0.45\ s$

(f) $t = 1.5\ s$
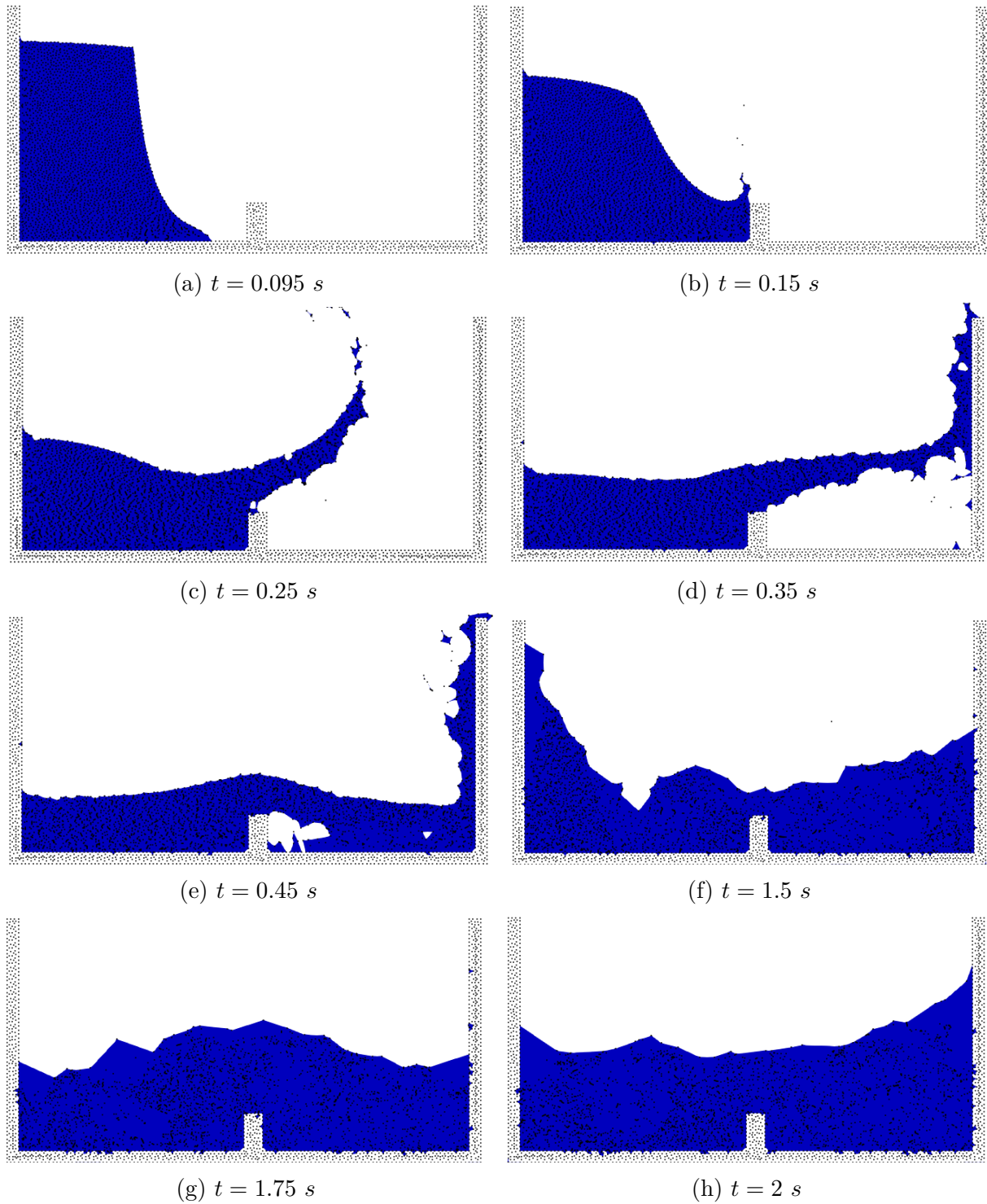

(g) $t = 1.75\ s$

(h) $t = 2\ s$

Figure 4.2: Collapse of a water column on a rigid object. At different time frames.

As mentioned previously, the comparison and validation of the results from the numerical simulation are carried out on the basis of the laboratory experience fond in [45], where its dimensions correspond to those of the numerical model in this case. The coarse mesh type was chosen for the sequence of images in figure 4.3 representing the identical times of the laboratory test, respectively $t = 0.05\ s$; $t = 0.1\ s$; $t = 0.2\ s$; $t = 0.3\ s$; $t = 0.4\ s$ and $t = 0.6\ s$. The fluid position and displacement information from each of the images is in good agreement and has sufficient accuracy, since the water behaviour towards the rigid obstacle in the numerical simulation is almost identical to that in the laboratory experiment.
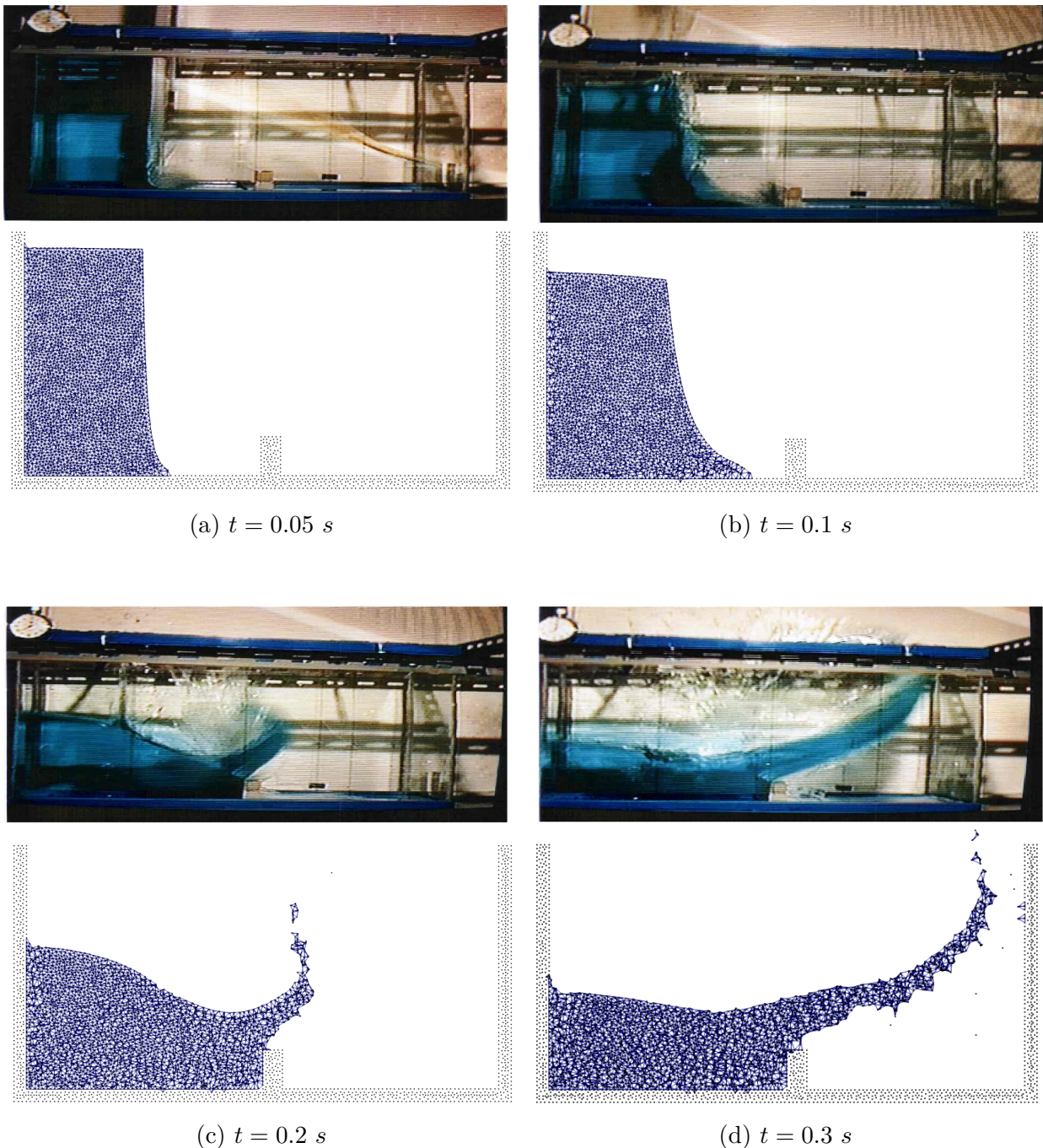

(a) $t = 0.05\ s$ (b) $t = 0.1\ s$

(c) $t = 0.2\ s$ (d) $t = 0.3\ s$

Figure 4.3: Dam break against a rigid step. Experimental[45] and numerical results.

<center>(a) $t = 0.4 \ s$ (b) $t = 0.6 \ s$</center>
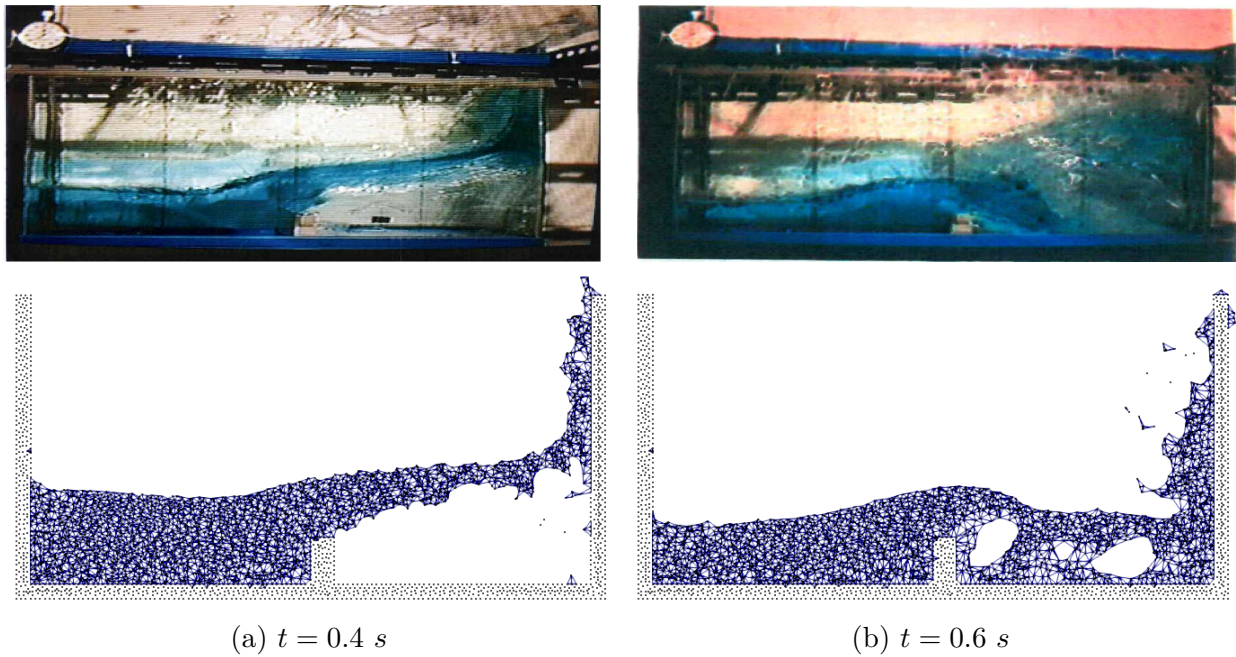
<center>Figure 4.3: Continued.</center>

To compare the time evolution of the pressure (P) at three different points of the rigid obstacle, exactly at the left bottom, middle and top of the solid obstacle, the following comparative plots are obtained as shown in 4.5. The laps of time taken for the water takes to reach the obstacle is clearly represented by the the zero pressure values at the beginning of the curves. A sudden increase in pressure is then observed when the fluid hits the obstacle, with the pressure being greater at the bottom, although the pressure peak is found in the centre with P $\approx$ 11500 Pa. Then the pressure decreases in the three points until until it stabilises between two values $P = 2500 \ Pa$ and $P = -1500 \ Pa$.
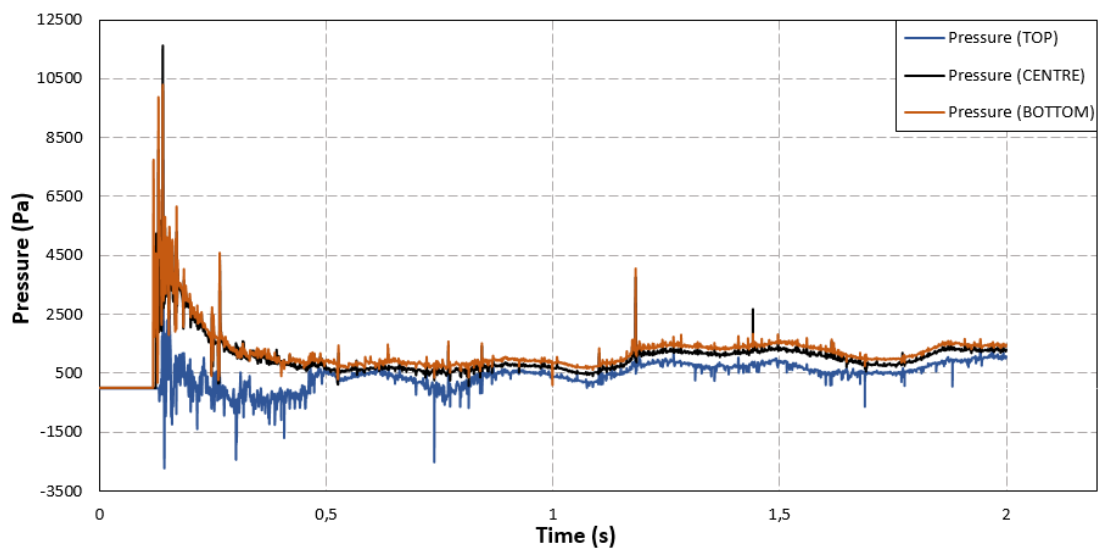

<center>Figure 4.5: Comparison of time evolution of pressure at 3 points of rigid obstacle.</center>

<center>40</center>

The figure 4.6, shows the pressure distribution at three selected time values ((a) $t =$ 0.1405 s, (b) $t = 0.3$ s and (c) $t = 2$ s) along a vertical cut line running through the left side of the obstacle. The line is drawn from the lower point of the rigid step to a height $H = 300$ mm, which corresponds to the height of the tank.
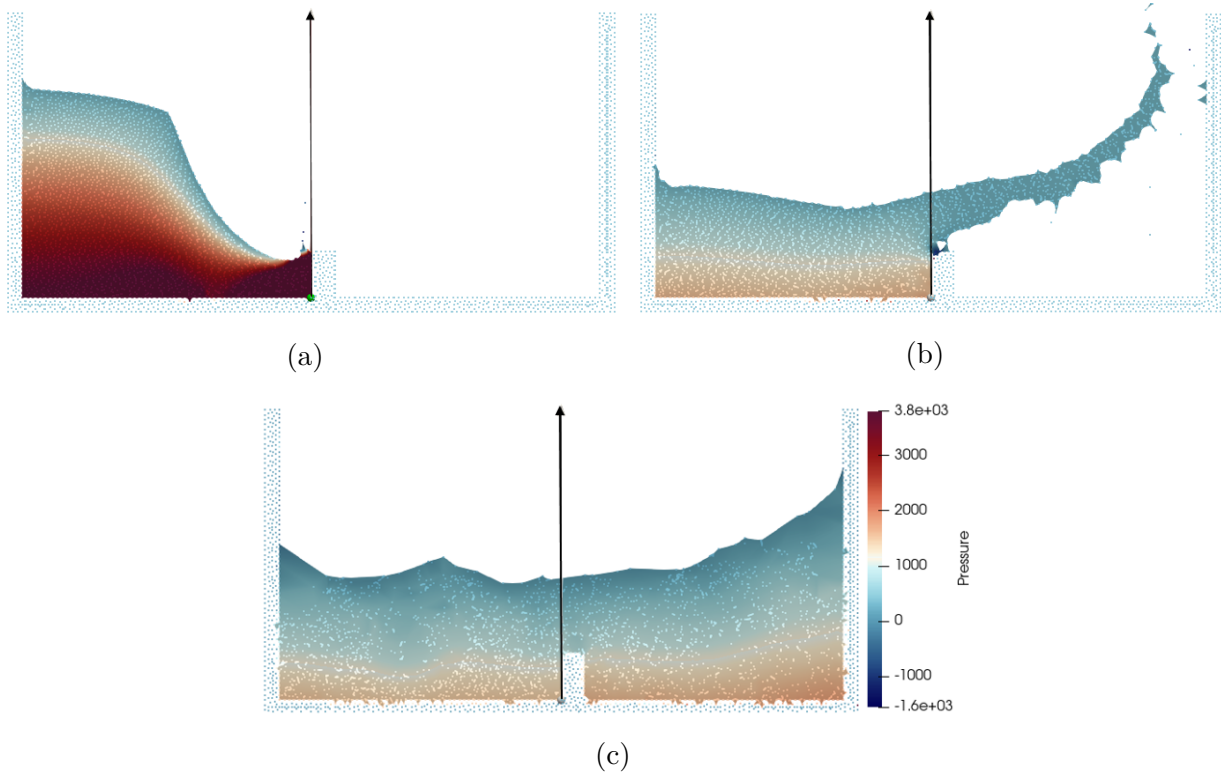

(a)

(b)

(c)

Figure 4.6: Pressure iso-values and cut-line representation at three time lines.

Plot in figure 4.7, displays the pressure distribution at $t = 0.1405$ s, along a cut line, i.e. at the time when the fluid reaches the entire left side of the rigid obstacle of height $H = 48$ mm, as shown in figure 4.6a. In the following graph, the pressure is shown only up to height $Y = 50$ mm, which clearly indicates the height of the obstacle along which the pressure is positive. The peak of the pressure distribution reaches a value of $P_{max} = 11500$ Pa at the centre of the obstacle. The total pressure force applied to the obstacle $F_p = 399.16$ N where is calculated numerically using the trapezoidal rule, where P_i is the pressure at the point of height Y_i:

$$F_p = \int_S p(y) \, \mathrm{d}y = \sum_i (P_{i+1} + P_i)(Y_{i+1} - Y_i) \tag{4.1}$$
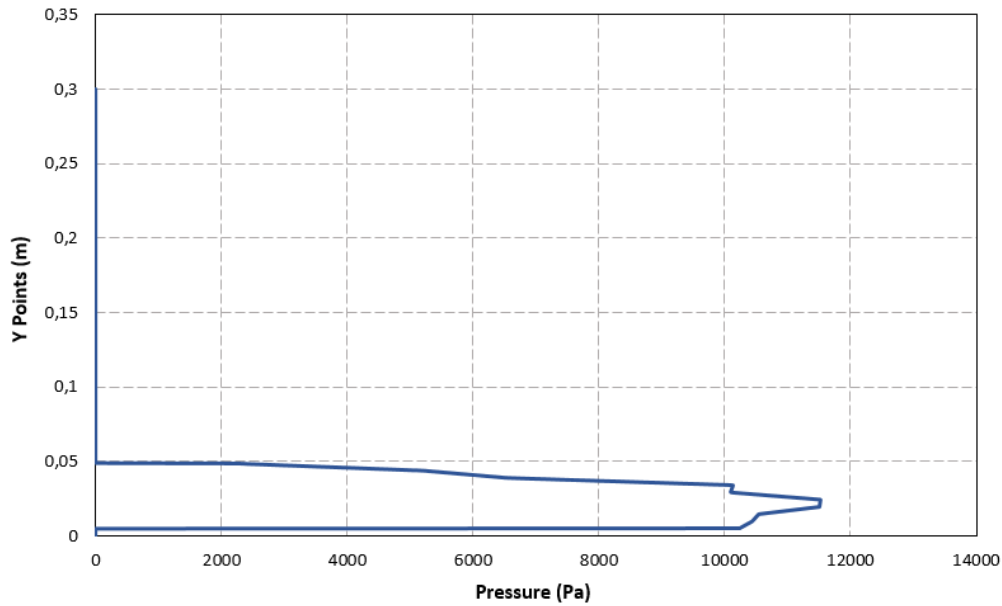
Figure 4.7: Pressure distribution at: $t = 0.1405\ s$, along a cut line.

Plot in figure 4.8, shows the pressure distribution at $t = 0.3\ s$, along the cut line. This is the time when the tongue water is formed when the fluid sprays higher after impacting the obstacle, as it is illustrated in figure 4.6b. In this plot, the pressure distribution has reached a value of $Y = 110\ mm$ of the line, showing the height that the water has attained along the vertical cut, and a maximum pressure value of $P_{max} = 1265\ Pa$ is observed at the lower part of the obstacle. It can also be noticed that negative pressures have occurred in a narrow region just above the top of the obstacle . It will be interesting to investigate this phenomenon in more detail. A total force due to the pressure is calculated and a value of $F_p = 46\ N$ is found, which is lesser than that of the previous distribution.
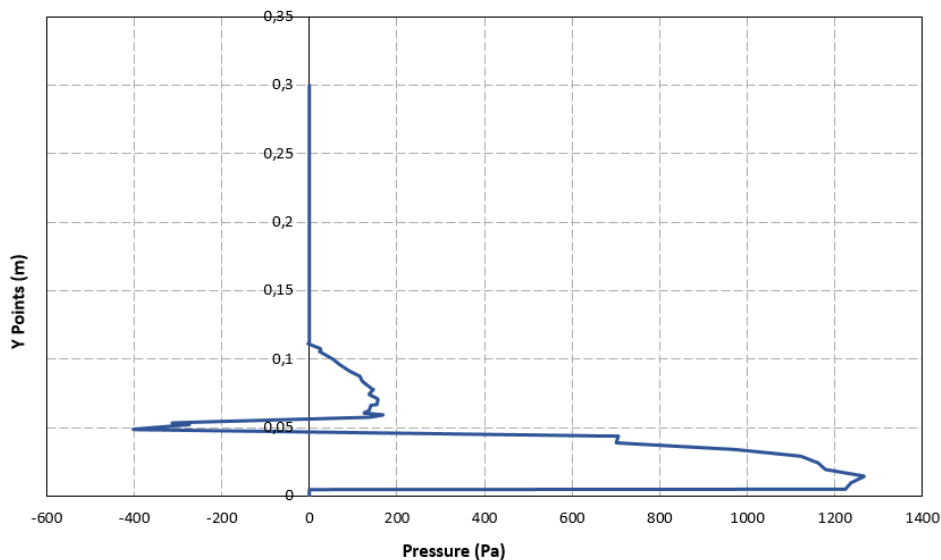

Figure 4.8: Pressure distribution at $t = 0.3\ s$, along a cut line.

Figure 4.9, shows the pressure distribution at $t = 2\ s$, along the same section line. This time has been chosen to represent the time when the sloshing water begins to settle and calm down, as shown in figure 4.6c. In this graph, the pressure has been recorded up to a value of $Y = 138\ mm$ of the vertical line, showing the height that the water has reached with the sloshing and wave motion hitting it, as well as a pressure peak value of $P_{max} = 1470\ Pa$. A total force due to pressure is calculated and a value of $F_p = 101.51\ N$ is found.
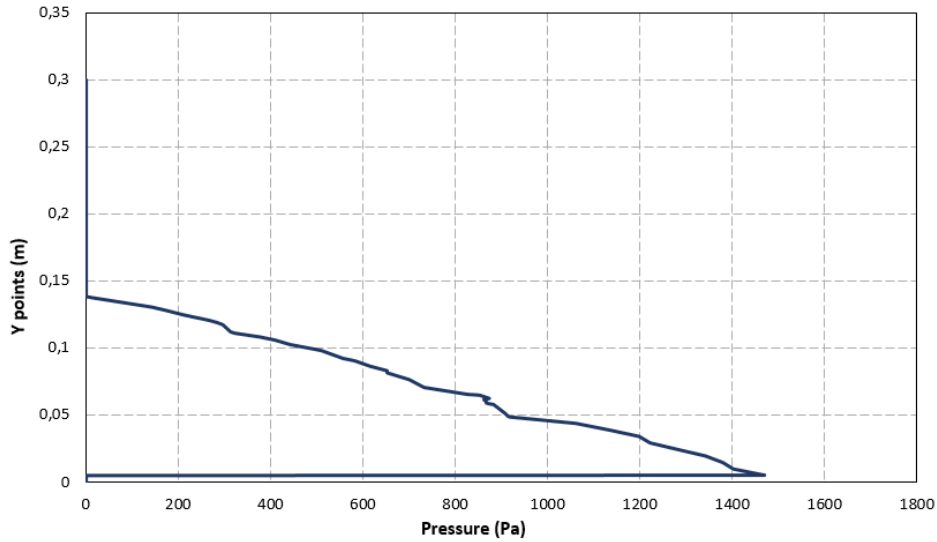

Figure 4.9: Pressure distribution at $t = 2\ s$, along a cut line.

4.3   Dam-break with elastic obstacle

The second case studied is the same collapse of the water column, only this time against an elastic obstacle, which is a typical reference problem for FSI analysis with free surface flow. The phenomenon is explained in these two subsections, starting with the theoretical analysis of the coupled problem and then the numerical results.

4.3.1   The coupled problem

In [25] it was explained that at the coupling boundary, the fluid and solid velocities should converge to the same value. This could be expressed as:

$$u_f|_{\Gamma_F} = u_s|_{\Gamma_S} \tag{4.2}$$

Therefore, two subsystems need to be considered, these being the fluid system:

$$F = \left(u_f^{n+1}, P^{n+1}, x_f^{n+1}, u_s^{n+1}, x_s^{n+1}\right) = 0 \tag{4.3}$$

and the solid system:

$$S = \left(u_s^{n+1}, x_s^{n+1}, u_f^{n+1}, P^{n+1}, x_f^{n+1} \right) = 0 \tag{4.4}$$

In the previous, only the variables to be solved at time step n+1 are indicated. An iterative procedure must be used to couple the two systems. A fixed-point algorithm can be introduced, thereby the system could be written:

$$\left(u_{f,k+1}^{n+1}, P_{k+1}^{n+1}, x_{f,k+1}^{n+1} \right) = N \left(u_{f,k}^{n+1}, P_k^{n+1}, x_{f,k}^{n+1}, u_s^{n+1}, x_s^{n+1} \right) \tag{4.5}$$

$$\left(u_{s,k+1}^{n+1}, x_{s,k+1}^{n+1} \right) = G \left(u_{s,k}^{n+1}, x_{s,k}^{n+1}, u_f^{n+1}, P^{n+1}, x_f^{n+1} \right) \tag{4.6}$$

The first equation denotes the fluid subsystem that was solved using PFEM, which was detailed in Chapter 2, and the second is the solid subsystem, in our present frame is a beam subsystem using FEM, likewise previously detailed in Chapter 3. The subscript k is the iteration counter. The Gauss-Sedel method is used within the OpenSeePy code to perform such iterations. Thus, the iterative procedure means that the first one of the two subsystems is solved, e.g. the fluid system. The information from the fluid calculation is then used to solve the solid system.

The equations 4.5 and 4.6 should be modified and the final expression to be used for the calculation is as follows:

$$\left(u_{f,k+1}^{n+1}, P_{k+1}^{n+1}, x_{f,k+1}^{n+1} \right) = N \left(u_{f,k}^{n+1}, P_k^{n+1}, x_{f,k}^{n+1}, u_{s,k}^{n+1}, x_{s,k}^{n+1} \right) \tag{4.7}$$

$$\left(u_{s,k+1}^{n+1}, x_{s,k+1}^{n+1} \right) = G \left(u_{s,k}^{n+1}, x_{s,k}^{n+1}, u_{f,k+1}^{n+1}, P_{k+1}^{n+1}, x_{f,k+1}^{n+1} \right) \tag{4.8}$$

Convergence is achieved when the difference between the velocities of successive iteration steps is less than the acceptable error.

4.3.2   Numerical Results

This second numerical application case is a well-known FSI model, originally proposed by [30], who used a constant space-time finite element formulation, which then became a commonly used FSI test case presented in the literature with different approaches, for example researchers in[24, 10, 50, 35, 7, 43], although the experimental data are not available, it provides a good point of comparison for the present simulation with these articles results.

As in the first case, this simulation is also carried out with a deformable mesh size and an alpha shape set to $\alpha = 1.4$, however this time with an average cell size of $h = 10\ mm$. The adaptive time step is kept between 10^{-6} and 10^{-3} for the time integration scheme, and the total duration of the analysis is $2\ s$.

The geometric and physical properties of the tank and the fluid given in the first example, namely water, are kept the same, only the obstacle is different, since it is an elastic obstacle fixed to the bottom of the tank, as shown in Figure 4.10. The deformable obstacle is a beam of height $H_e = 80\ mm$ having a density of $\rho_s = 2500\ kg/m^3$, a modulus of elasticity of $E = 10^6\ Pa$ and a Poisson's ratio of $\nu = 0$.
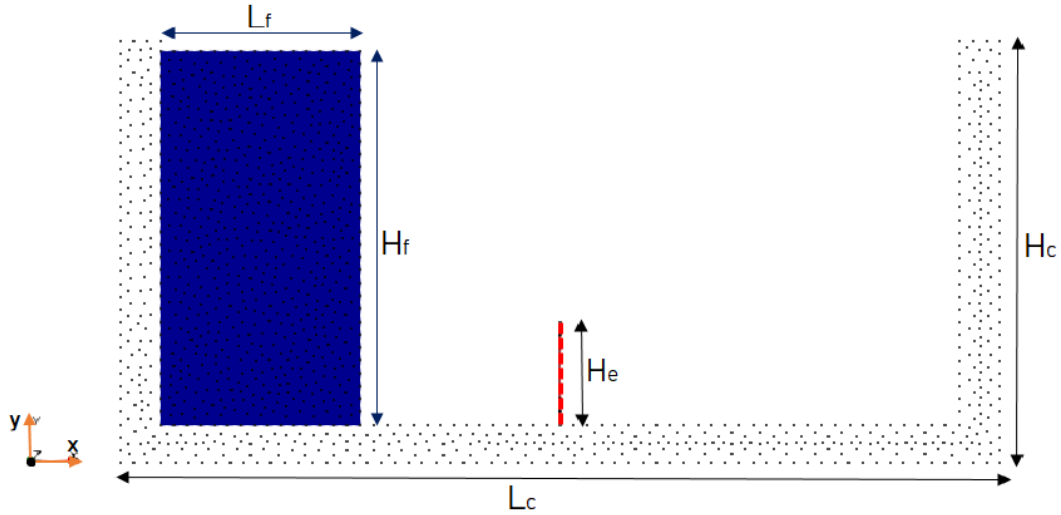

Figure 4.10: Collapse of a water column on an elastic obstacle. Initial geometry of the problem.

Figure 4.11, shows snapshots of the second case of dam break simulation, with an elastic obstacle at different time stages $t = 0.1\ s$; $t = 0.2\ s$; $t = 0.3\ s$; $t = 0.4\ s$; $t = 0.5\ s$; $t = 0.6\ s$; $t = 0.8\ s$ and $t = 2\ s$, using a refined mesh.

The water column, initially on the left, collapses under the effect of gravity after the immediate removal of the vertical wall, leaving the water to flow and to propagate along the rectangular channel, as shown in figure 4.11a. It then hits the elastic obstacle in the lower part, which immediately deflects slightly to the left at $t = 0.145\ s$, then as the fluid rises and climbs over the structure, which makes it deflect strongly to the right as figure 4.11b shows. A tongue of water forms, as seen in figure 4.11c, at which point the beam pushes the water back and begins to deflect to the left as a result of the fluid striking the left wall. The water reaches the right wall of the tank at time $t = 0.4\ s$ and falls under gravity, trapping air underneath, which then fills the tank and starts to slosh between the right and left walls, creating waves that constantly impact on the elastic obstacle, causing it to continue to bend between the two directions (figures 4.11e, 4.11f and 4.11g), although not as strongly as before. At $t = 2\ s$ it can be observed that the sloshing slows down and the beam becomes stable, since the waves no longer hit it with the same intensity and straightness as before. At the end, the water stops sloshing and stabilises at a value of H_{ff} which is calculated to correspond to the theoretical value of $H_{ff} = 73\ mm$, that is not included here because the simulation time chosen is a brief one of $2\ s$.

(a) $t = 0.1 \ s$

(b) $t = 0.2 \ s$

(c) $t = 0.3 \ s$

(d) $t = 0.4 \ s$

(e) $t = 0.5 \ s$

(f) $t = 0.6 \ s$
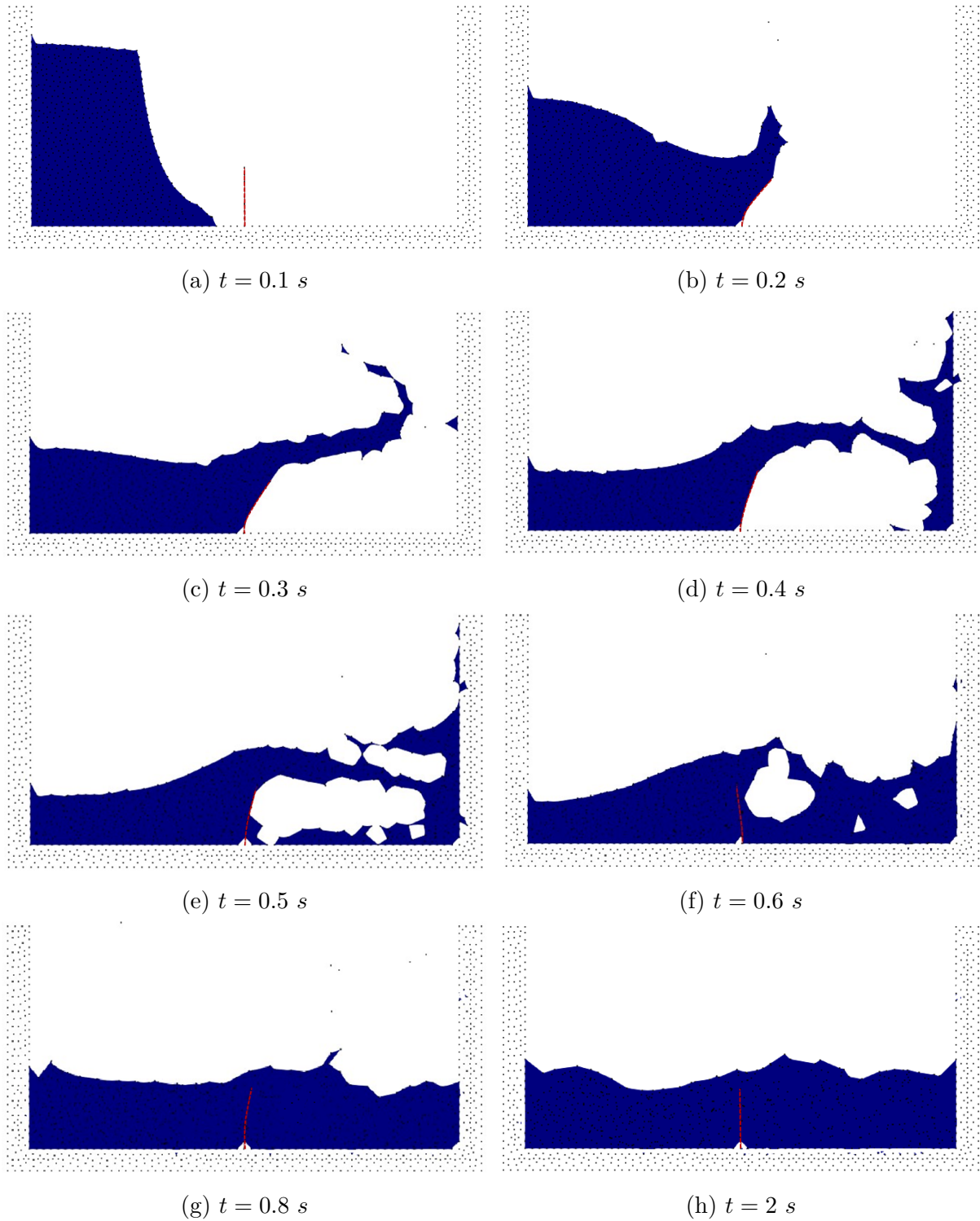
(g) $t = 0.8 \ s$

(h) $t = 2 \ s$

Figure 4.11: Collapse of a water column on an elastic object. At different time frames.

A comparative study is carried out by plotting the evolution over time at three different points of the beam, specifically at the upper, middle and lower ends of the left side of the elastic obstacle. In addition to the time evolution of the pressure, this example also gives the time evolution of the horizontal and vertical displacement of the beam.

The time evolution of the horizontal displacement of the three points of the beam is shown in 4.12. Where the displacement is first observed at the lower point just after the fluid-structure impact, although the graph shows no change, this is simply because it's almost unnoticeable next to the two upper points. A maximum of the value of the x-displacement is found at the top of the beam with $x = 0.048\ m$ at $t = 0.24\ s$, in general the first and second point displacement diagrams give the same curvature, but with the values of the upper horizontal displacement being greater, while the displacement at the bottom of the beam is almost undetectable as it is fixed there just below.
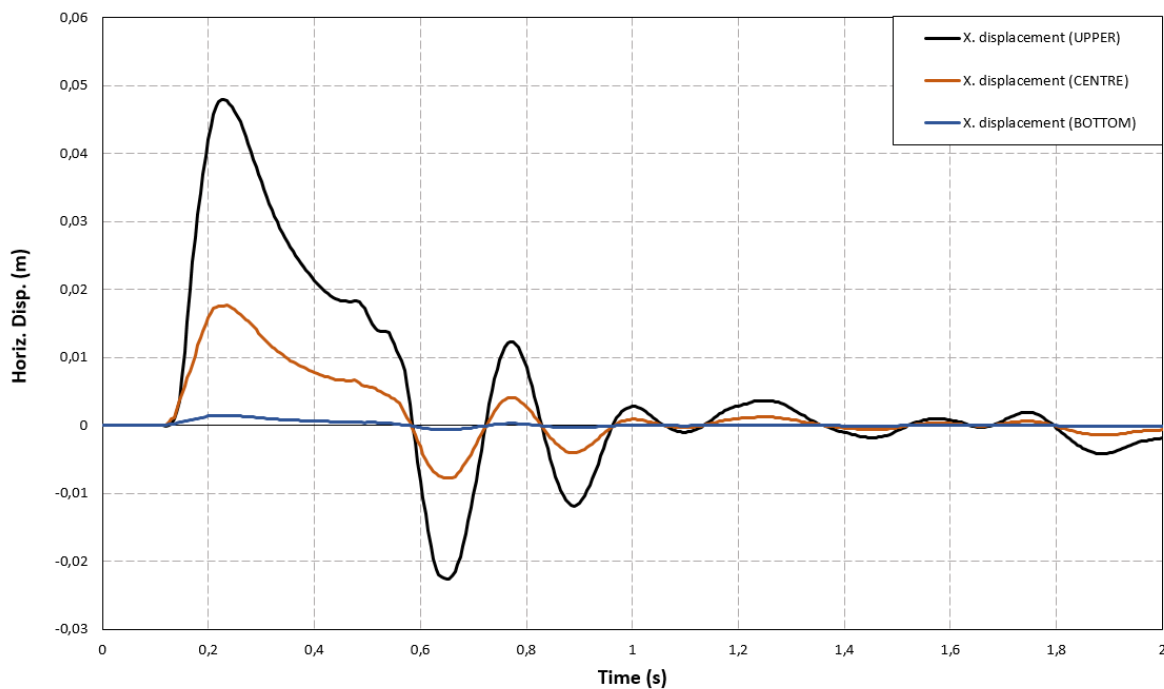

Figure 4.12: Comparison of time evolution of horizontal displacement at 3 beam points.

The graph 4.13, represents a comparison of the time evolution of the vertical displacement at the same three points of the beam, where a great similarity with the graph 4.12 is observed, with the values obtained at the top being greater than those of the centre, the graph of these two having almost the same pattern, and also at the bottom, where it is also difficult not to say that there is no vertical displacement. The maximum value of the y-displacement due to the banding is detected at $t = 0.23\ s$ with $Y = -0.019\ m$, where the negative sign means that the beam bends backwards and then tries to return to its original shape, obtaining values close to zero, until it stabilises and no vertical displacement is recorded.
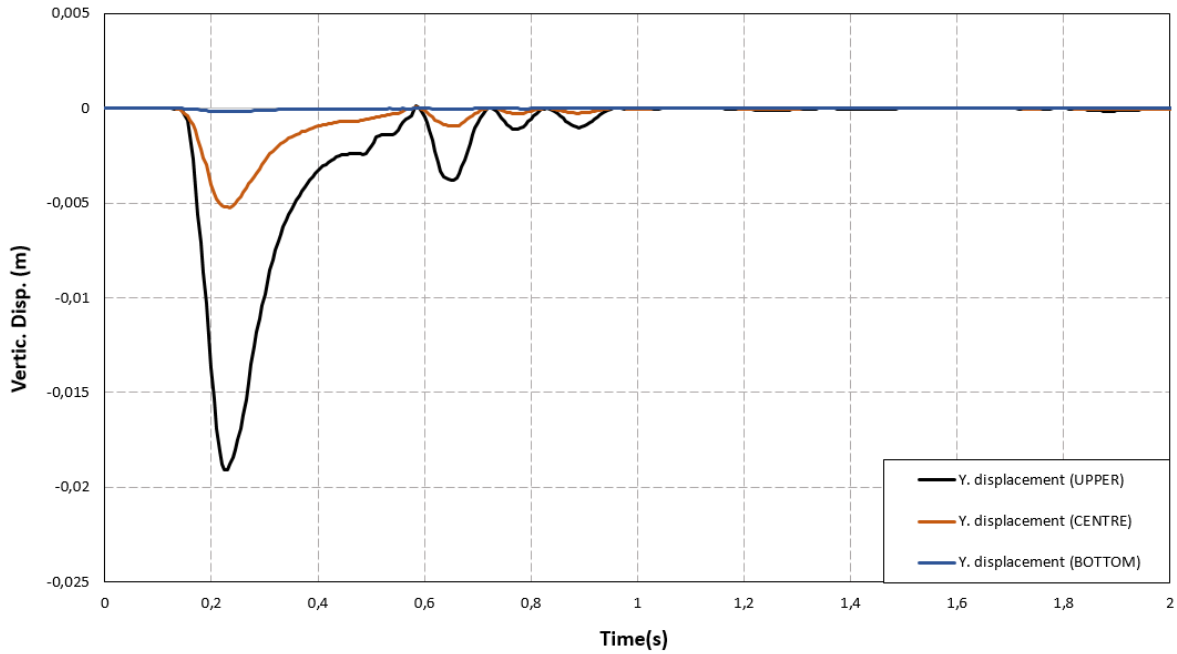
Figure 4.13: Comparison of time evolution of vertical displacement at 3 beam points.

In 4.14, the pressure is recorded immediately after the impact at the bottom, where its peak is also recorded with a value of $P = 4750\ Pa$ at $t = 0.57\ s$, then the centre values are obtained, ending with those of the upper point. After a while, when the sloshing of the water in the tank calms down, the pressure is found to be between $P = 0\ Pa$ and $P = 1000\ Pa$.
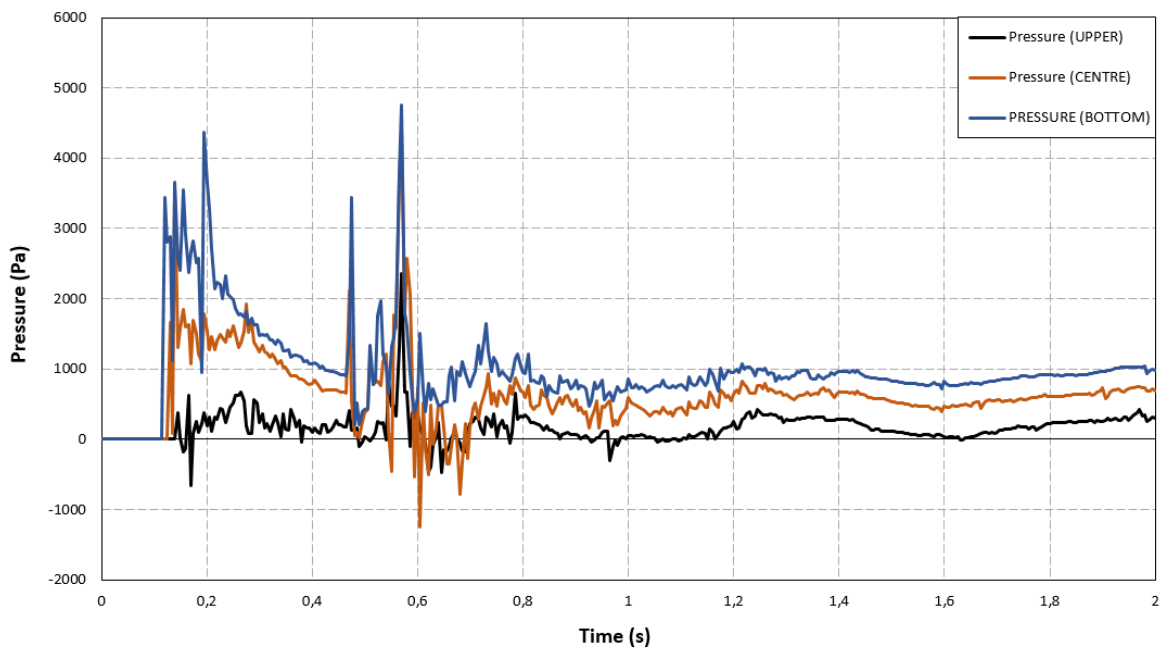

Figure 4.14: Comparison of time evolution of pressure at 3 beam points.

As already mentioned, the experimental data for this example are not available; in order to validate the present simulation, a comparison is conducted of the time evolution of the horizontal displacement at the upper point of the beam together with the results presented by Idelsohn & Onate [24], Meduri [35], Cerquaglia [7] and Zhu & Scott [50] in the same sense of the X-displacement at the left corner of the elastic obstacle, as the Figure 4.15 indicates.
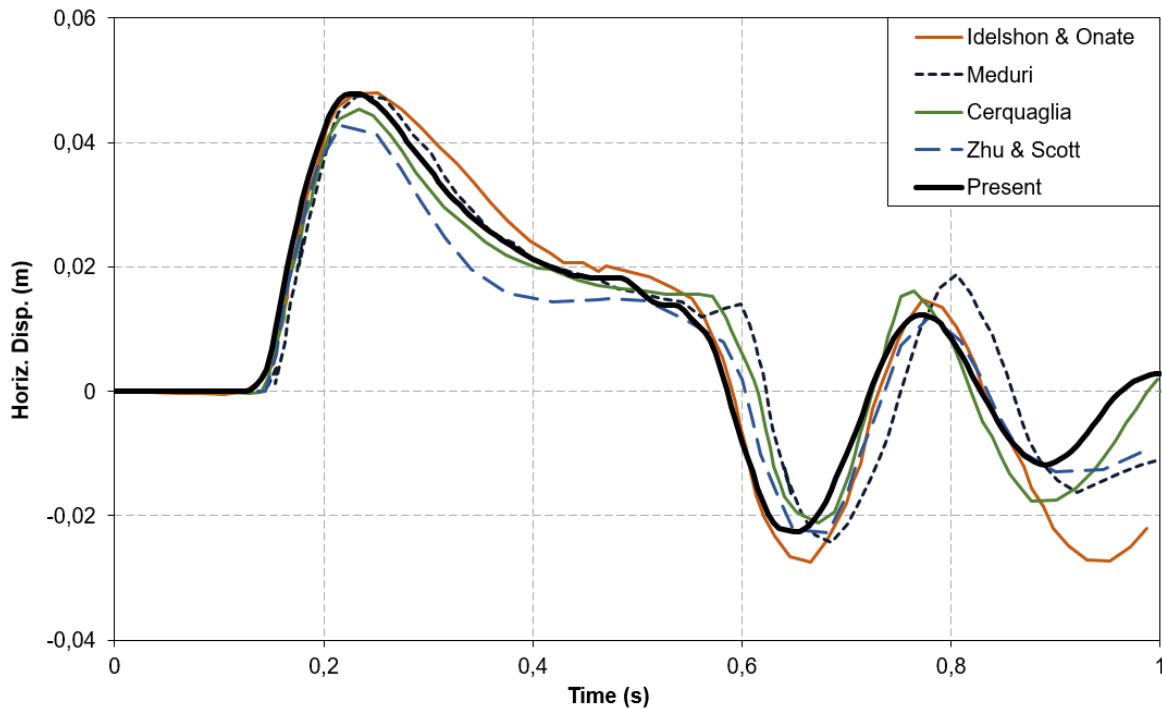

Figure 4.15: Comparisons of the horizontal displacement of the beam tip with different references results.

By examining the plots in Figure 4.15, the motions of the fluid and the elastic obstacle can be divided into four stages, as well as the comparison between results can be drawn in each of these stages.

- The first stage from $t = 0$ s to $t = 0.13$ s, when the water column has started to collapse but the water flow has not yet reached the elastic obstacle, where a good agreement can be extracted among all plots.

- The second stage is at times greater than $t = 0.13$ s and less than $t = 0.23$ s, in this stage the water has hit the elastic obstacle causing it to deflect to the right until $t = 0.23$ s when the deviation reaches its peak, a general similarity can be obtained with all the other values, although the present results and those of Idelsohn & Onate are quasi the same, where the fluid reached the obstacle at the same instant as this one, which is a little earlier than the rest which are at $t = 0.14$ s as well as the maximum of deviation is the same for these two and the one of Meduri $X = 0.048$ m at $t = 0.23$ s while it is less for Cerquaglia and Zhu & Scott $t = 0.045$ m and $t = 0.042$ m respectively.

- The third stage is at times larger than $t = 0.23 \ s$ and shorter than $t = 0.65 \ s$, during this stage the collapse of the water column comes almost to an end and the deformation of the elastic obstacle is gradually restored, while the fluid flow continues to move forward towards the right side wall. From $t = 0.23 \ s$ to $t = 0.55 \ s$ there is a great resemblance between the present simulation values and those of Meduri, while from $t = 0.55 \ s$ the similarity with the values of Idelsohn & Onate is observed, although the minimum value is the same as that of Zhu & Scott $X = -0.022 \ m$ at $t = 0.65 \ s$ in contrast to the results of Idelsohn & Onate $X = -0.023 \ m$ at $t = 0.68 \ s$ and Meduri $X = -0.027 \ m$ at $t = 0.66 \ s$, whose minimum is greater and with Cerquaglia $X = -0.020 \ m$ at $t = 0.67 \ s$ it is less. The negative sign indicates the deflection of the flexible obstacle to the left when the fluid falls as it hits the right wall, which fills the tank, causing it to return to the left as it hits the obstacle bouncing it to the left.

- The last stage is at times larger than $t = 0.65 \ s$, during which the reflected water waves from the right side wall hit the elastic obstacle, causing it to oscillate right and left under the influence of the water flow. The values obtained from the simulation are in good accordance with those found in Idelsohn & Onate and Zhu & Scott.

Despite some differences with the reference results, which also differ to the same extent among themselves, the overall time evolution of the response here compares well with the literature, leading to a confirmation of the validation of the simulation and its accuracy.

The following figure 4.16, illustrates the pressure distribution along a vertical section line at four selected times: (a) $t = 0.145 \ s$, the time when the water hit the bottom of the flexible obstacle, causing it to deflect to the left for a very brief period, (b) $t = 0.23 \ s$, the time when the maximum deflection of the beam to the right was recorded, (c) $t = 0.65 \ s$, chosen to represent the time of the maximum deflection of the obstacle to the left, and at (d) $t = 2 \ s$, when the elastic obstacle returns to its stable form. As in the previous example, the line is drawn from the lowest point of the elastic obstacle to the tank height $H = 300 \ mm$ and the total force due to pressure is also calculated using equation 4.1. In this case, the total force due to the velocity across the deflected obstacle is also calculated, which can be numerically determined using the trapezoidal rule, where V_{xi} is the horizontal velocity along the beam at the given time:

$$F_v = \int_0^b \rho g V_x^2 \ \mathrm{d}y = \rho g \sum_i V_{xi}^2 \tag{4.9}$$

(a) $t = 0.145\ s$ (b) $t = 0.23\ s$

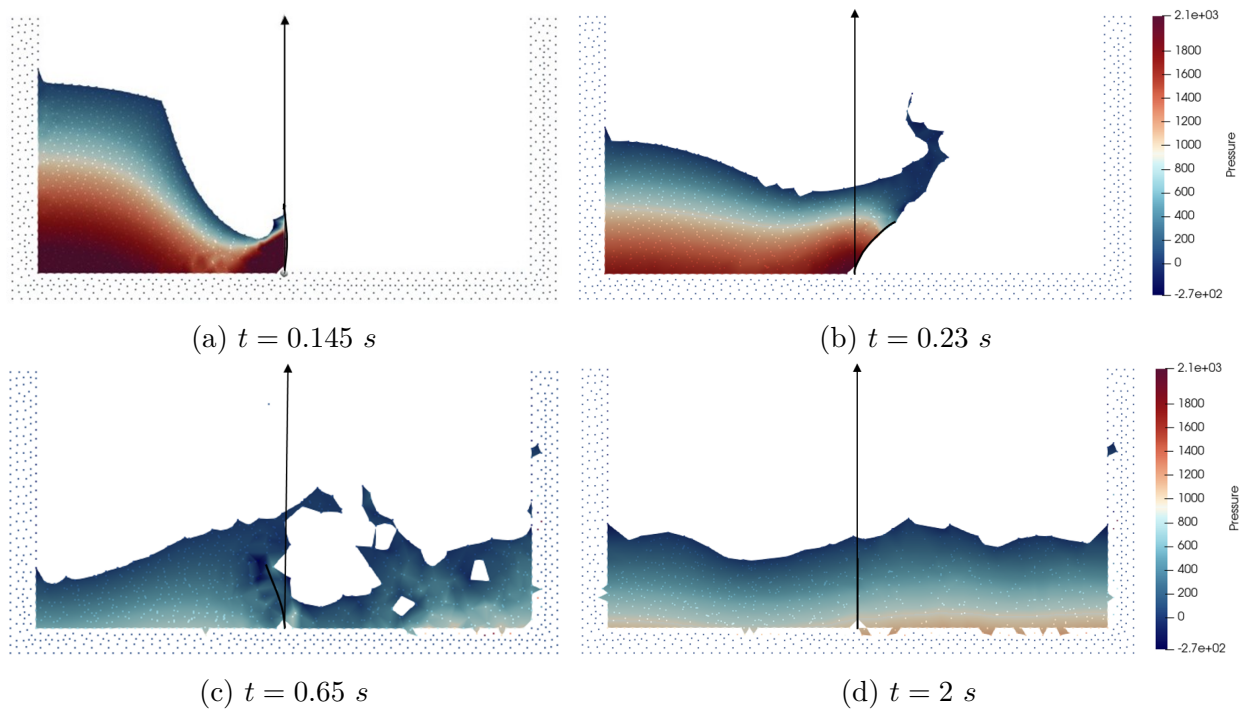(c) $t = 0.65\ s$ (d) $t = 2\ s$

Figure 4.16: Pressure iso-values and cut-line representation at four time lines.

Graph 4.17, shows the pressure distribution at $t = 0.145\ s$ along a section line shown in figure 4.16a. In this plot, the pressure has been recorded up to a value of $Y = 0.076\ m$ of the vertical line with a maximum pressure at $Y = 0.01\ m$ of value $P_{max} = 2570\ Pa$. The total force due to the pressure is determined as $F_p = 84.14\ N$ and the total force due to the velocity across the deflected beam is obtained of a value of $F_v = 7005.94\ N$.
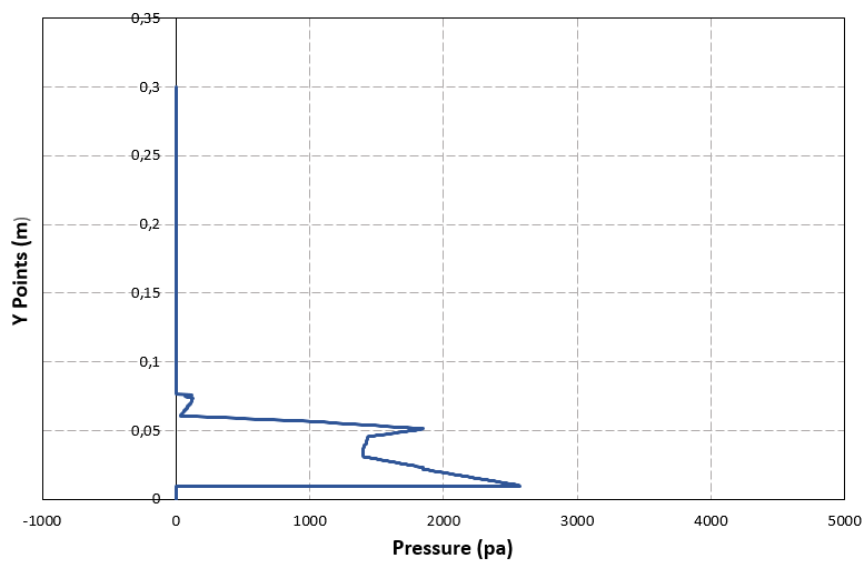

Figure 4.17: Pressure distribution at $t = 0.145\ s$, along a cut line.

Figure 4.17, shows the plot of the pressure distribution at $t = 0.145 \; s$ along a cut line shown in figure 4.16a. In this graphic, the pressure has been recorded up to a value of $Y = 0.076 \; m$ of the vertical line with a maximum pressure at $Y = 0.01 \; m$ of value $P_{max} = 2570 \; Pa$. The total force due to the pressure is calculated to be $F_p = 102.8 \; N$ and the total force due to the velocity across the deflected beam is $F_v = 2.527 \; N$.
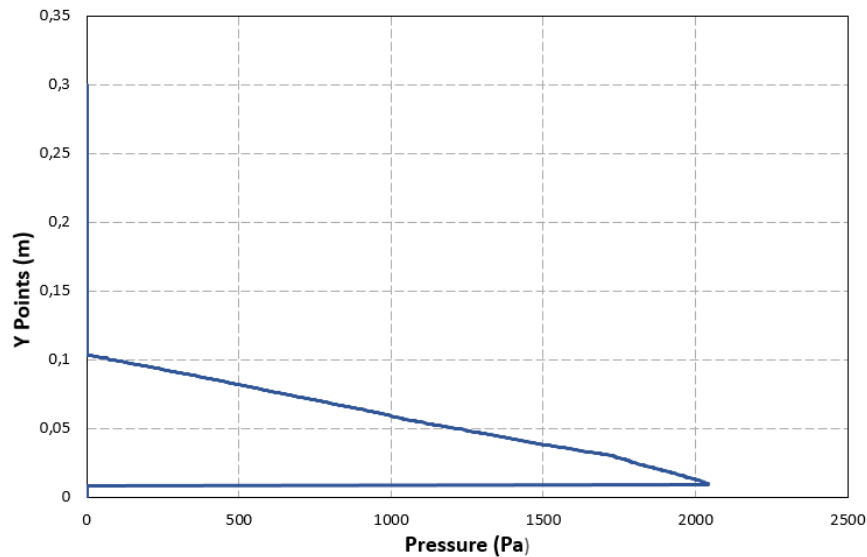

Figure 4.18: Pressure distribution at $t = 0.23 \; s$, along a cut line.

Graph 4.19, shows the pressure distribution at $t = 0.65 \; s$ along a section line shown in figure 4.16c. In this plot, the pressure has been recorded up to a value of $Y = 0.137 \; m$ of the vertical line with a maximum pressure at $Y = 0.01 \; m$ of value $P_{max} = 551 \; Pa$. The total force due to the pressure is determined as $F_p = 8.34 \; N$ and the total force due to the velocity across the deflected beam is obtained of a value of $F_v = 13.95 \; N$.
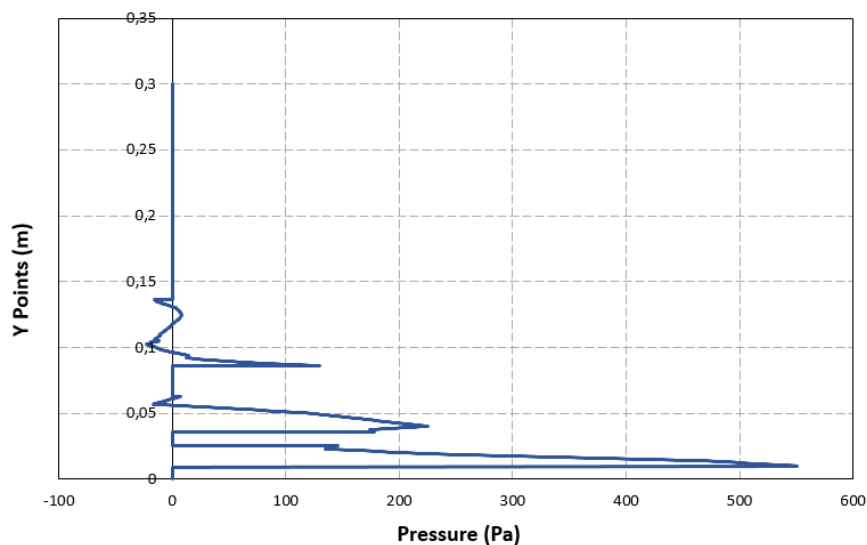

Figure 4.19: Pressure distribution at $t = 0.65 \; s$, along a cut line.

The graph in figure 4.20 presents the pressure distribution at $t = 0.145\ s$ along the section line given in figure 4.16d. In this graph the pressure is recorded up to a value of $Y = 0.106\ m$ of the vertical line with a peak pressure $P_{max} = 1010\ Pa$ at $Y = 0.00\ m$. The total force due to the pressure is $F_p = 51.75\ N$ and the total force due to the velocity across the deflected beam is determined to be $F_v = 347.23\ N$.
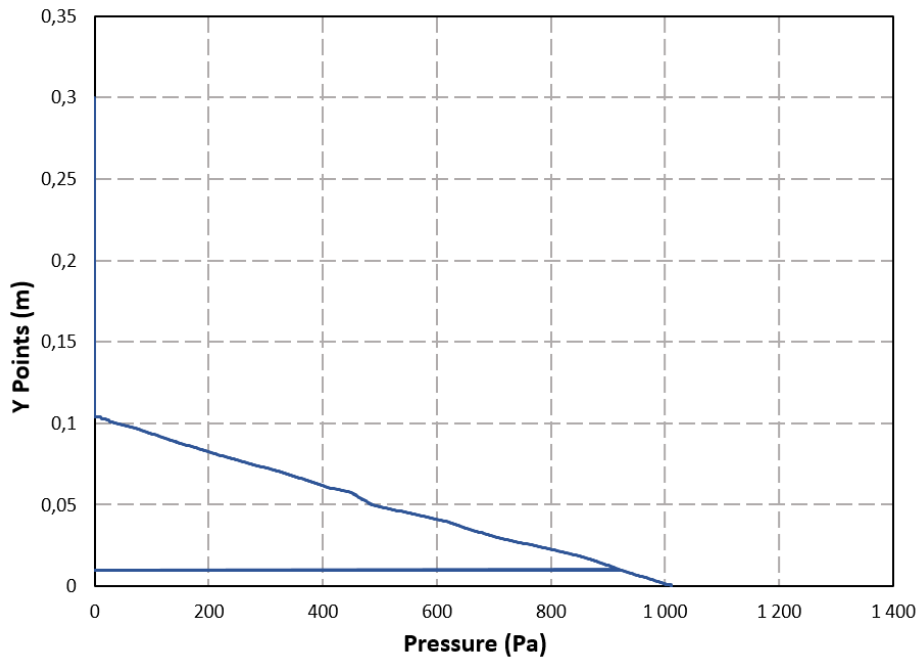

Figure 4.20: Pressure distribution at $t = 2\ s$, along a cut line.

4.4   Conclusion

In this chapter, the concepts of the previous chapters are put into practice in the two simple examples of dam break with obstacle. The results of the visualisation of PFEM in the examples is exploded where the reaction of the fluid with the two obstacles is almost identical in the two analysis. Although the performance of the obstacle is totally different in these two cases where the rigid obstacle remains still only pressure is recorded while in the elastic obstacle, different proprieties are recorded such as the horizontal and vertical displacement along side the pressure. A validation of these two simulations can be drawn, since the comparison with the experimental test of the rigid obstacle and the time history of the horizontal tip displacement of the elastic obstacle with the simulations of the aforementioned researchers resulted in a good agreement, demonstrating the success of these simulations presented in this project.

Conclusion

The dam break phenomenon is a well-known example of an unstable and fast-moving flow that is extensively studied in the field of research, not only because of the threats that its release represents to the human life and the economy of countries, but also because it provides a rigorous and evidence-based validation test for numerical models given the multiplicity of phenomena associated with it, such as the transport of mass and energy. A common case of this problem is the dam break against a flexible obstacle, which is mentioned in almost every discussion of fluid-structure interaction, and has been the focus of this project, thus providing an opportunity to review some of the fluid mechanics concepts presented in Chapter 1.

This project simulated two cases of dam break against an obstacle, one against a fixed obstacle and the other against a flexible one. The equations for the fluid in motion (Navier-Stokes equations) were described in a Lagrangian framework, a 21st century numerical method explained in Chapter 2, was chosen because it represents a modern approach, although it was invented in 2004 and it is one of the particle methods referred to as Particle Finite Element Method, but the solution method is novel. The bending behaviour of the elastic obstacle under the effect of the fluid flow is represented by a 2D element beam, for which the governing equation has been treated with the Finite Element Method, as previously explained in Chapter 3, using a simple but effective example.

The numerical simulation of the two cases shown in Chapter 4 put into practice all the concepts of the previous three chapters. Using OpenSeesPy scripting, the shape of the fluid on the two obstacles and the beam deflection were visualised and studied using ParaView. The results of the simulation showed a great similarity between these two examples in the way the fluid reacted from splashing to sloshing in the tank, although the response of the obstacles was completely different. In the case of the rigid obstacle, only the time evolution of the hydrodynamic pressure is recorded, unlike the beam obstacle where the time history of the vertical and horizontal displacements were also recorded along with the pressure evolution. In both tests the pressure along a cut line was also examined at certain times.

In order to verify the accuracy of the two simulations, a comparison study was carried out. For the dam break test with the rigid obstacle, there is a laboratory experiment in [45], so the comparative analysis of the two led to a good agreement. In the case of the flexible obstacle test, the experimental data are not yet available for this exact example, which many researchers have used in this situation to compare the time history of the horizontal displacement at the left side of the tip of the obstacle between each other, so here the same has been done with the literature [24, 50, 35, 7] and also a good correspondence has been found. These two results of the comparisons have marked the validation of the two simulations presented in this project.

In conclusion, the fluid-structure interaction case seen in this project is just one of many more existing, as well as the method applied to analyse this particular example is just a basic model in which there are many other methods that may not obtain exactly the same results, as each method has its unique characteristics and errors. However, with certainty, the results obtained can be judged as correct, as there are numerous references that have found almost the identical results, taking into consideration the differences in the resources employed to arrive at this particular conclusion.

Bibliography

[1] AHMADI, S. M., AND YAMAMOTO, Y. A new dam-break outflow-rate concept and its installation to a hydro-morphodynamics simulation model based on fdm (an example on amagase dam of japan). *Water 13*, 13 (2021).

[2] ALLAH TOHAMY, A. S. A. Critical shear stresses for web of plate girder subjected to shear loading and contained cut-outs. Master's thesis, Minia University, Minya, Egypte, 06 2015.

[3] ANDERSSON, B., ANDERSSON, R., HÅKANSSON, L., MORTENSEN, M., SUDIYO, R., AND VAN WACHEM, B. *Computational fluid dynamics for engineers*. Cambridge university press, 2011.

[4] AURELI, F., DAZZI, S., MARANZONI, A., MIGNOSA, P., AND VACONDIO, R. Experimental and numerical evaluation of the force due to the impact of a dam-break wave on a structure. *Advances in Water Resources 76* (2015), 29–42.

[5] AURELI, F., MARANZONI, A., PETACCIA, G., AND SOARES-FRAZÃO, S. Review of experimental investigations of dam-break flows over fixed bottom. *Water 15* (03 2023), 1229.

[6] BRITANNICA, T. E. o. E. Elasticity. https://www.britannica.com/science/elasticity-physics, 2022.

[7] CERQUAGLIA, M.-L., THOMAS, D., BOMAN, R., TERRAPON, V., AND PONTHOT, J.-P. A fully partitioned lagrangian framework for fsi problems characterized by free surfaces, large solid deformations and displacements, and strong added-mass effects. *Computer Methods in Applied Mechanics and Engineering 348* (2019), 409–442.

[8] CLINE, D. Variational principles in classical mechanics. https://LibreTexts.org)a, 02 2021.

[9] CODINA, R. Pressure stability in fractional step finite element methods for incompressible flows. *Journal of Computational Physics 170*, 1 (2001), 112–140.

[10] CREMONESI, M., FRANCI, A., IDELSOHN, S., AND OÑATE, E. A state of the art review of the particle finite element method (pfem). *Archives of Computational Methods in Engineering 27* (08 2020).

[11] DAI, Z., WANG, F., HUANG, Y., SONG, K., AND IIO, A. Sph-based numerical modeling for the post-failure behavior of the landslides triggered by the 2016 kumamoto earthquake. *Geoenvironmental Disasters 3* (11 2016).

[12] DONEA, J., HUERTA, A., PONTHOT, J.-P., AND RODRÍGUEZ-FERRAN, A. *Arbitrary Lagrangian–Eulerian Methods.* John Wiley and Sons, Ltd, 2004, ch. 14.

[13] FRANCI, A., AND CREMONESI, M. On the effect of standard pfem remeshing on volume conservation in free-surface fluid flow problems. *Computational particle mechanics 4*, 3 (2017), 331–343.

[14] GAPPER, J., AND SERRANO, A. An implementation of the sph method and its application to two-dimensional dam break cases. *Ingeniería Investigación y Tecnología 24* (01 2023), 1–11.

[15] GHORAI, S., AND NIGAM, K. Cfd modeling of flow profiles and interfacial phenomena in two-phase flow in pipes. *Chemical Engineering and Processing: Process Intensification 45*, 1 (2006), 55–65.

[16] GHOUINI, F. Calcul des écoulements intationnaires à surface libre (onde de rupture de barrage). Master's thesis, University Abderrahmane MIRA, Bejaia, Algeria, 09 2017.

[17] GREAVES, D. M. Simulation of viscous water column collapse using adapting hierarchical grids. *International Journal for Numerical Methods in Fluids 50*, 6 (2006), 693–711.

[18] GUZ, A. N. *Elastic solids.* Springer Berlin Heidelberg, Berlin, Heidelberg, 1999, pp. 63–91.

[19] IDELSOHN, S., OÑATE, E., AND ALBERTO STORTI, M. Lagrangian formulations to solve free surface incompressible inviscid fluid flows. *Computer Methods in Applied Mechanics and Engineering 191*, 6 (2001), 583–593.

[20] IDELSOHN, S., OÑATE, E., CELIGUETA, M., AND SUÁREZ, B. *The Particle Finite Element Method (PFEM). An Effective Numerical Technique for Solving Marine, Naval and Harbour Engineering Problems*, vol. 29. Springer Netherlands, 01 2013, pp. 65–81.

[21] IDELSOHN, S., OÑATE, E., AND DEL PIN, F. The particle finite element method; a powerful tool to solve incompressible flows with free-surfaces and breaking waves. *Numerical Methods in Engineering 61* (10 2004), 964–989.

[22] IDELSOHN, S., OÑATE, E., DEL PIN, F., AND AUBRY, R. The particle finite element method. an overview. *International Journal of Computational Methods 1* (09 2004), 267–307.

[23] IDELSOHN, S., OÑATE, E., AND MONICA, M.-T. Multi-fluid flows with the particle finite element method. *Computer Methods in Applied Mechanics and Engineering 198*, 33 (2009), 2750–2767.

[24] IDELSOHN, S. R., MARTI, J., LIMACHE, A., AND OÑATE, E. Unified lagrangian formulation for elastic solids and incompressible fluids: application to fluid–structure interaction problems via the pfem. *Computer Methods in Applied Mechanics and Engineering 197*, 19-20 (2008), 1762–1776.

[25] IDELSOHN, S. R., OÑATE, E., DEL PIN, F., AND CALVO, N. Fluid–structure interaction using the particle finite element method. *Computer methods in applied mechanics and engineering 195*, 17-18 (2006), 2100–2123.

[26] JEONG, W., AND SEONG, J. Comparison of effects on technical variances of computational fluid dynamics (cfd) software based on finite element and finite volume methods. *International Journal of Mechanical Sciences 78* (2014), 19–26.

[27] JO, J. C. Fluid-structure interactions. *Korea institute of Nuclear safety, Republic of Korea* (2004).

[28] KLEINSTREUER, C. *Biofluid dynamics: Principles and selected applications.* CRC Press, 2006.

[29] KÖLKE, A. *Modelling and discretisation of moving discontinuities in boundary-coupled multi field system.* PhD thesis, Technical University Carolo-Wilhelmina of Braunschweig, Germany, 2005.

[30] KÖLKE, A., WALHORN, E., HÜBNER, B., AND DINKLER, D. Fluid–structure coupling within a monolithic model involving free surface flows. *Computers & Structures 83* (09 2005), 2100–2111.

[31] KOSHIZUKA, S., SHIBATA, K., KONDO, M., AND MATSUNAGA, T. Chapter 1 - introduction. In *Moving Particle Semi-implicit Method*, S. Koshizuka, K. Shibata, M. Kondo, and T. Matsunaga, Eds. Academic Press, 2018, pp. 1–23.

[32] LEURS, T. The particle finite element method: Two alternative formulations. Master's thesis, Eindhoven University of Technology, 2007.

[33] LIND, S. J., ROGERS, B. D., AND STANSBY, P. K. Review of smoothed particle hydrodynamics: towards converged lagrangian flow modelling. *Proceedings of the royal society A 476*, 2241 (2020), 20190801.

[34] LIU, M., AND LIU, G. Smoothed particle hydrodynamics (sph): an overview and recent developments. *Archives of Computational Methods in Engineering 17* (03 2010), 25–76.

[35] MEDURI, S., CREMONESI, M., PEREGO, U., BETTINOTTI, O., KURKCHUBASCHE, A., AND OANCEA, V. A partitioned fully explicit lagrangian finite element method for highly nonlinear fluid-structure interaction problems. *International Journal for Numerical Methods in Engineering 113*, 1 (2018), 43–64.

[36] PAI, D. S.-I. *Two-Phase Flow*, vol. 3. Friendr. Vieweg and SohnVerlagsgesllschafz mbH, Braunschweig, Germany, 1977.

[37] RAJA, R. S. Coupled fluid structure interaction analysis on a cylinder exposed to ocean wave loading. Master's thesis, Chalmers University of Technology, Göteborg, Sweden, 2012.

[38] REDDY, J. N. A dual mesh finite domain method for the numerical solution of differential equations. *International Journal for Computational Methods in Engineering Science and Mechanics 20*, 3 (2019), 212–228.

[39] RODRÍGUEZ-FERRAN, A., PÉREZ-FOGUET, A., AND HUERTA, A. Arbitrary lagrangian–eulerian (ale) formulation for hyperelastoplasticity. *International Journal for Numerical Methods in Engineering 53*, 8 (2002), 1831–1851.

[40] SEGHIR, A. Cours of finite element method. Tech. rep., Dept. of Hydraulics, University of A-Mira Bejaïa, 2014.

[41] SOULI, M., AND ZOLESIO, J. Arbitrary lagrangian–eulerian and free surface methods in fluid mechanics. *Computer Methods in Applied Mechanics and Engineering 191*, 3 (2001), 451–466.

[42] STEPHEN, L., AND JOSE, A. An overview of surface tracking and representation in fluid simulation. *International Journal of Advanced Computer Science and Applications 6* (11 2015).

[43] SUN, Z., HUANG, Z., AND ZHOU, X. Benchmarking the material point method for interaction problems between the free surface flow and elastic structure. *Progress in Computational Fluid Dynamics, an International Journal 19*, 1 (2019), 1–11.

[44] THE REGENTS OF THE UNIVERSITY OF CALIFORNIA. https://opensees.github.io/OpenSeesDocumentation/index.html#, 2022.

[45] UBBINK, O. *Numerical prediction of two fluid systems with sharp interfaces.* PhD thesis, Imperial College of Science, Technology & Medicine, London, UK, 1997.

[46] VACONDIO, R., ALTOMARE, C., DE LEFFE, M., HU, X., LE TOUZÉ, D., LIND, S., MARONGIU, J.-C., MARRONE, S., ROGERS, B. D., AND SOUTO-IGLESIAS, A. Grand challenges for smoothed particle hydrodynamics numerical schemes. *Computational Particle Mechanics 8* (2021), 575–588.

[47] ZHANG, C., ZHU, Y., WU, D., AND HU, X. Review on smoothed particle hydrodynamics: Methodology development and recent achievement. *arXiv preprint arXiv:2205.03074* (2022).

[48] ZHANG, H., GUO, X.-W., LI, C., LIU, Q., XU, H., AND LIU, J. Accelerating fvm-based parallel fluid simulations with better grid renumbering methods. *Applied Sciences 12*, 15 (2022).

[49] ZHU, M. https://openseespydoc.readthedocs.io/en/latest/index.html#, 2019-2022.

[50] ZHU, M., AND SCOTT, M. H. Improved fractional step method for simulating fluid-structure interaction using the pfem. *International Journal for Numerical Methods in Engineering 99*, 12 (2014), 925–944.